National Library of Canada

Acquisitions and Bibliographic Services Branch

395 Wellington Street
Ottawa, Ontario
K1A 0N4

Bibliothèque nationale du Canada

Direction des acquisitions et des services bibliographiques

395, rue Wellington
Ottawa (Ontario)
K1A 0N4

Your file Votre référence

Our file Notre référence

NOTICE

The quality of this microform is heavily dependent upon the quality of the original thesis submitted for microfilming. Every effort has been made to ensure the highest quality of reproduction possible.

If pages are missing, contact the university which granted the degree.

Some pages may have indistinct print especially if the original pages were typed with a poor typewriter ribbon or if the university sent us an inferior photocopy.

Reproduction in full or in part of this microform is governed by the Canadian Copyright Act, R.S.C. 1970, c. C-30, and subsequent amendments.

AVIS

La qualité de cette microforme dépend grandement de la qualité de la thèse soumise au microfilmage. Nous avons tout fait pour assurer une qualité supérieure de reproduction.

S'il manque des pages, veuillez communiquer avec l'université qui a conféré le grade.

La qualité d'impression de certaines pages peut laisser à désirer, surtout si les pages originales ont été dactylographiées à l'aide d'un ruban usé ou si l'université nous a fait parvenir une photocopie de qualité inférieure.

La reproduction, même partielle, de cette microforme est soumise à la Loi canadienne sur le droit d'auteur, SRC 1970, c. C-30, et ses amendements subséquents.

Canada

Study of Excitonic Superfluidity in Cu_2O

by

Eric Benson

Thesis submitted to the
Faculty of Graduate Studies and Research
in partial fulfillment of the requirements
of the Master of Science in Physics

Department of Physics
University of Ottawa
150 Louis Pasteur
Ottawa, Ontario
K1N 6N5

National Library
of Canada

Acquisitions and
Bibliographic Services Branch

395 Wellington Street
Ottawa, Ontario
K1A 0N4

Bibliothèque nationale
du Canada

Direction des acquisitions et
des services bibliographiques

395, rue Wellington
Ottawa (Ontario)
K1A 0N4

Your file Votre référence

Our file Notre référence

ISBN 0-612-07789-6

Canada

UNIVERSITÉ D'OTTAWA
UNIVERSITY OF OTTAWA

Abstract

Excitonic transport measurements in ultra-pure semiconducting Cu_2O crystals were performed over a wide range of exciton densities at liquid Helium temperatures. The excitons were created with a high power pulsed Nd:YAG laser in the Cu_2O over a 3 mm^2 area and in a thin layer a few micrometers thick. The excitons then migrated over several millimeters through the crystal and were measured at the opposite sample face in time resolve using the exciton mediated photovoltaic effect. At low exciton density the transport is diffusive as expected and the results are well fitted by a diffusion equation. However at high exciton densities the transport becomes ballistic and a reduction in the size of the exciton distribution becomes apparent. Furthermore, the density at which there is a crossover from diffusive to ballistic behaviour follows a $T^{3/2}$ temperature dependence and is of the same order of magnitude as the predicted critical density for Bose-Einstein condensation. Pump-probe experiments with two laser pulses separated by a variable time delay allowed the formation of two exciton packets separated by the distance traveled by the first packet during the time delay. The experiments confirmed the attractive nature of a Bose condensate with other condensates and normal Bose particles, and revealed the formation of a soliton condensate. We conclude that the results presented in this work are consistent with the condensation and superfluid transport of excitons in Cu_2O.

Sommaire

Des mesures de transport excitonique dans un cristal pur de Cu_2O ont été effectuées à diverses densités excitoniques aux températures de l'hélium liquide. Les excitons ont été créés au moyen d'un laser pulsé Nd:YAG à haute puissance dans le Cu_2O sur une superficie de 3 mm^2 et en une mince couche d'une épaisseur de quelques micromètres. Les excitons se sont propagés sur plusieurs millimètres à travers le cristal et ont été mesurés en temps résolu, à la surface opposée de l'échantillon en utilisant l'effet photovoltaïque. À basse densité excitonique, le transport est diffus tel que prévu et les résultats correspondent à ceux que produit une équation de diffusion. Toutefois, à de hautes densités excitoniques, le transport est balistique et une réduction de la dispersion des particules est évidente. De plus, la densité à laquelle il y a passage d'un régime diffusif à un comportement balistique varie en fonction de la température selon $T^{3/2}$ et est du même ordre de grandeur que prédit par la théorie Bose-Einstein. Des expériences de type pompe-sonde utilisant deux pulses lasers à délai variable ont créé deux paquets excitoniques que séparait la distance parcourue par le premier paquet au cours du délai établi. Les expériences confirment l'effet d'attraction d'un condensat Bose avec d'autres condensats et avec des particules de Bose normales. Elles démontrent également qu'il y a formation d'un soliton condensé. Nous concluons que les résultats présentés dans cette thèse sont conformes à la condensation des excitons et à leur transport superfluide dans le Cu_2O.

Acknowledgments

Foremost I would like to thank Dr. Fortin for his support and patience for what has become a very involving and intriguing project. I would also like to thank A. Mysyrowicz for the many useful discussions over the course of this project. Also I must thank P. Demerdjiev, G. Lafrenière and S. Fafard for their help during the experiments.

Statement of Originality

All of the results presented in this thesis are from measurements completed at the University of Ottawa by the author in collaboration with E. Fortin and A. Mysyrowicz. Some of the results printed in this thesis were published in the following papers:

Excitonic Superfluidity in Cu_2O, A. Mysyrowicz, E. Fortin, S. Fafard, E. Benson and G. Lafrenière, in Quantum Electronics and Laser Science Conference, 1993 OSA Technical Digest Section B 3, 67.

Excitonic Superfluidity in Cu_2O, E. Fortin, E. Benson and A. Mysyrowicz, *Bose-Einstein Condensation*, ed. A. Griffin, D. Snoke and S. Stingari, Cambridge University Press, 519 (1995).

Soliton Propagation of Excitonic Packets and Superfluidity in Cu_2O, A. Mysyrowicz, E. Fortin, E. Benson, S. Fafard and E. Hanamura, Solid State Communications 92, 957, (1994).

Table of Contents

List of Figures

Introduction

Under special conditions, Bose-Einstein statistics predict that integer spin particles will undergo a transition to a new phase of matter. This phase called the condensed phase, exhibits unusual properties such as superfluidity originating from the macroscopic occupation of a single quantum level.

Bose-Einstein condensation has long been suspected to be the principal cause of the λ-transition observed in He at 2.17K. However, the important particle interactions between the closely spaced atoms in the liquid and the inability to control the particle density make it very difficult to distinguish Bose statistical effects. A more dilute, variable density system is sought to verify the properties of a nearly ideal Bose gas. An excellent candidate is a gas of excitonic particles created by optical absorption in an ultra-pure semiconducting Cu_2O crystal. The small exciton mass and radius, coupled with the unusually long lifetime ($\tau \approx 10$ μsec) of the para variety of excitons in Cu_2O allow for the observation of a stable variable density dilute Bose gas. Previous measurements [1, 2, 3, 4, 5] sought to uncover Bose condensation of excitons in Cu_2O by measuring the photoluminescence produced by these particles as they decay. However these measurements were limited to non-equilibrium conditions at early times after exciton formation (<50 nsec) and because of this and other reasons explained in section 2.2.1, the results did not clearly demonstrate the presence of an excitonic condensate.

The focus of this work is shifted from optical to electrical detection of the excitons at much later times (~1 μsec) than in previous experiments. Using the exciton mediated photovoltaic effect at a Cu/Cu_2O Schottky barrier, optically inactive long lived paraexcitons are detected far from their inital location. The experiments described here will explore the transport of excitons over macroscopic distances (several millimeters) with exciton densities covering eight orders of magnitude. Diffusive transport at exciton densities of about 10^{11} cm^{-3} will be studied in steady state after which diffusive and ballistic

transport at densities approaching 10^{19} cm^{-3} will be measured in time resolved spectroscopy.

The layout of this thesis is as follows. The theoretical background covering the behaviour of ideal Bose gases will be introduced, along with the properties of a condensate. The energy band structure of semiconducting crystals and excitons will be reviewed and the particular properties of the excitons in Cu_2O will be discussed with respect to Bose condensation. The preparation for the experiments, such as laser calibration, sample preparation and experimental setup will be described, along with characterization of the exciton detector. The final section will present and describe the experimental results. The analysis of these results will show that a break in the otherwise linear behaviour of exciton cloud properties as a function of particle density, follows a $T^{3/2}$ temperature dependence and that the anomalous ballistic or superfluid transport over macroscopic distances is consistent with Bose condensation of excitons in Cu_2O. Further measurements and analysis will reveal the attractive interaction of an exciton condensate with normal excitons and with other condensates.

1 - Theory

1.1 Bosons and condensation

1.1.1 Bosons and Fermions

At extremely low temperatures or very high densities the true quantum nature of particles is revealed. In this strange realm, classical statistics i.e. Maxwell-Boltzmann statistics, must be reformulated to take into account the fundamental quantum interactions occurring between individual particles. The interactions observed between indistinguishable quantum particles are governed by the particle wave functions. Particles whose wave function is odd under particle exchange

$$\psi(\mathbf{r}_1, \mathbf{r}_2) = -\psi(\mathbf{r}_2, \mathbf{r}_1) \tag{1}$$

are called fermions, and those with even wave functions are labeled bosons.

$$\psi(\mathbf{r}_1, \mathbf{r}_2) = \psi(\mathbf{r}_2, \mathbf{r}_1) \tag{2}$$

Empirically, fermions have been known to be half-integer spin particles, while bosons are integer spin particles. The symmetry of the particle wave functions leads to the two basic properties of fermions and bosons. Fermions are restricted from having more than one particle occupy a single quantum state, while the number of bosons in the same quantum state is unlimited. From this basic boson characteristic flows the spectacular properties of a superfluid.

1.1.2 Ideal Bose Gas

An ideal Bose gas is a system where quantum statistics are the dominant factor in the behaviour of the particles but where particle interactions are negligible. The ideal gas model closely resembles the experimentally observed exciton system to be introduced later. Predictions about the basic properties of an ideal quantum gas can be made when carefully examining the equations of state. To derive the equations of state for an ideal

Bose gas, we must start with the boson partition function $\mathcal{L}$, in the Grand Canonical Ensemble.

$$\mathcal{L}(z,V,T)=\sum_{N=0}^{\infty} z^N e^{-\beta\Sigma\varepsilon_{\mathbf{p}}f_{\mathbf{p}}}=\prod_{\mathbf{p}}\left[\sum_{f_{\mathbf{p}}}(ze^{-\beta\varepsilon_{\mathbf{p}}})^{f_{\mathbf{p}}}\right] \tag{3}$$

where N is the total number of particles, V is the volume, T is the temperature, $f_{\mathbf{p}}$ is the occupation number of a state with energy $\varepsilon_{\mathbf{p}}$, $\mathbf{p}$ is the momentum, β is equal to $1/k_BT$ and z is the fugacity. The fugacity of a gas is it's *"tendency to flee"* and is related to the chemical potential, μ of the gas ($z=e^{\beta\mu}$). The total number of particles is limited by the condition $\Sigma f_{\mathbf{p}}=N$, since the sum of the occupation numbers must give the total number of particles. For bosons $f_{\mathbf{p}}$ is any positive integer since there can be an unlimited number of particles in any state. Therefore the sum over $f_{\mathbf{p}}$ in Eq. (3) is a geometric series ($\sum_{s=0}^{\infty} r^s = 1/(1-r)$) reducing the partition function for bosons to

$$\mathcal{L}(z,V,T)=\prod_{\mathbf{p}}\frac{1}{1-ze^{-\beta\varepsilon_{\mathbf{p}}}}$$

The equations of state are

$$\frac{PV}{k_BT}=\log\mathcal{L}(z,V,T)=-\sum_{\mathbf{p}}\log(1-ze^{-\beta\varepsilon_{\mathbf{p}}}) \tag{4}$$

$$N=z\frac{\partial}{\partial z}\log\mathcal{L}(z,V,T)=\sum_{\mathbf{p}}\frac{ze^{-\beta\varepsilon_{\mathbf{p}}}}{1-ze^{-\beta\varepsilon_{\mathbf{p}}}} \tag{5}$$

In the limit as $V\to\infty$ the possible values of $\mathbf{p}$ form a continuum and the sum over $\mathbf{p}$ in Eqs. (4) and (5) is replaced by an integration such that $\Sigma_{\mathbf{p}}\to V\cdot(2s+1)/h^3\int d^3p$ where s is the particle spin and h is Planck's constant. The prefactor $V\cdot(2s+1)/h^3$ is due to the fact that allowable values of $\mathbf{p}$ form a cubic lattice in momentum space with a lattice constant $2\pi\hbar/(L(2s+1))$ where $L=V^{1/3}$, which approaches 0 as $V\to\infty$. Thus, as $V\to\infty$, a volume element of size d^3p in momentum space contains $(V(2s+1)/h^3)d^3p$ lattice points (or momentum states). Rewriting Eqs. (4) and (5):

$$\frac{P}{k_B T} = -\frac{4\pi \cdot (2s+1)}{h^3}\int_0^\infty dp p^2 \log(1 - ze^{-\beta p^2/2m}) - \frac{1}{V}\log(1-z) \tag{6}$$

$$n = \frac{4\pi \cdot (2s+1)}{h^3}\int_0^\infty dp p^2 \frac{1}{z^{-1}e^{\beta p^2/2m} - 1} + \frac{1}{V}\frac{z}{1-z} \tag{7}$$

Here we see that the ground state term has been split off from the sum before converting to an integral. This is an important and necessary step when dealing with bosons since the ground state term may be as important as the entire sum. Integrating Eq. (6) and (7) we get the following two equations which describe the relation between pressure, P, density, n, temperature, T and fugacity, z, for an ideal Bose gas:

$$\frac{P}{kT} = \frac{(2s+1)}{\lambda^3} g_{5/2}(z) - \frac{1}{V}\log(1-z) \tag{8}$$

$$n = \frac{(2s+1)}{\lambda^3} g_{3/2}(z) + \frac{1}{V}\frac{z}{1-z} \tag{9}$$

where $\lambda = \sqrt{2\pi\hbar^2 / mk_B T}$. The function $g_n(z)$ is defined as the sum $g_n(z) \equiv \sum_{l=1}^{\infty} z^l / l^n$.

The average occupation number as a function of temperature for bosons in an ideal gas can also be calculated using the partition function

$$< f_p >= -\frac{1}{\beta}\frac{\partial}{\partial \varepsilon_p}\log \mathcal{L} = \frac{ze^{-\beta\varepsilon_p}}{1 - ze^{-\beta\varepsilon_p}} \tag{10}$$

For the ground state (ε_p=0) the average occupation number $<f_0>$, is simply $z/(1-z)$, therefore we can rewrite Eq. (9) as

$$\frac{< f_o >}{V} = n - \frac{(2s+1)}{\lambda^3} g_{3/2}(z) \tag{11}$$

where $g_{3/2}(z)$ is a monotonically increasing function over the range $0 \leq z \leq 1$ with a maximum of $\cong 2.612$ for $z = 1$. Equation 11 implies that there is a finite fraction of particles occupying the ground state when the density and temperature are such that

$$n > \frac{(2s+1)}{\lambda^3} g_{3/2}(1) \tag{12}$$

This macroscopic occupation of the ground state is termed Bose-Einstein condensation. We can now define a critical density above which particles in the ground state of an ideal

Bose gas at a fixed temperature will condense into a new phase of matter.

$$n_c = 2.612 \cdot (2s+1) \cdot \left(\frac{mk_B}{2\pi\hbar^2}\right)^{3/2} T^{3/2} \tag{13}$$

The fraction of particles in the condensate at a temperature given by λ can be found by rearranging the terms in Eq. (11) and dividing both sides by the density n, giving

$$\frac{<f_o>}{N} = 1 - \frac{(2s+1)}{n\lambda^3} g_{3/2}(z) \tag{14}$$

We now replace $g_{3/2}(z)$ by $g_{3/2}(1)$ since for the condensed fraction to be non-zero, z must be one. Using Eq. (12) for fixed n, $g_{3/2}(1)=n\lambda_c^3/(2s+1)$ where λ_c is calculated at the critical temperature T_c and substituting this result into Eq. (14) we obtain

$$\frac{<f_o>}{N} = \begin{cases} 1-\left(\frac{T}{T_c}\right)^{3/2} & T \le T_c \\ 0 & T \ge T_c \end{cases} \tag{15}$$

Equation 15 is represented graphically in Fig. 1, and it can be seen that a finite fraction of particles are in the ground state for $T<T_c$. It can also be shown by evaluating terms of the summation in Eq. (5) as $V\rightarrow\infty$ that $<f_p>/N$ is always zero for $p\neq 0$. Therefore, for $T>T_c$, no energy level is occupied by a finite fraction of all the particles, and the particles are said to be "spread thinly" over all levels. For $T<T_c$, a finite fraction of particles $1-(T/T_c)^{3/2}$ occupies the level $p=0$ while the rest of the particles are spread thinly over all the excited states.

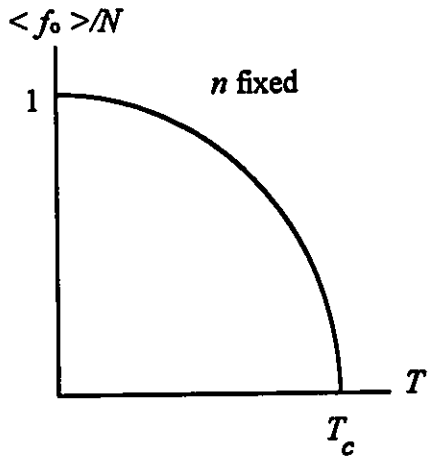

Fig. 1 Average occupation of the ground state as a function of temperature.

The pressure in the condensate can be found using Eq. (8) instead of (9) as a starting point. The last term of Eq. (8) can be ignored since it is of order $\log(N)$ whereas the first term is of order N. This means that no particle in the ground state ($\varepsilon_p=0$) can

contribute to the pressure for any z. Using the same procedure as above, the pressure P as a function of T is

$$P = \begin{cases} g_{5/2}(z)\cdot(2s+1)\cdot k_B T/\lambda^3 & n < n_c \\ 1.342\cdot(2s+1)\cdot k_B T/\lambda^3 & n > n_c \end{cases} \qquad (16)$$

where $g_{5/2}(1) \cong 1.342$ for $n > n_c$. A plot of the ideal Bose gas pressure versus particle density for several temperatures is shown in Fig. 2. The critical pressure for BEC is shown by the dashed line which is proportional to $n^{5/3}$. The relation between critical pressure and particle density can be obtained by substituting T=cst·$n^{2/3}$ from Eq. (13) into Eq. (16) for z=1. The most notable feature in Fig. 2 is the saturation of the gas pressure as a function of density beyond the BEC transition. This break in the behaviour of the pressure as a function of particle density is an indication of the change of phase, from gas to condensate, undergone by the particles. Such breaks in the behaviour should be apparent in all the physical properties of the gas after the transition, notably, the rate of expansion of the gas, and also its transport properties as explained in the next section.

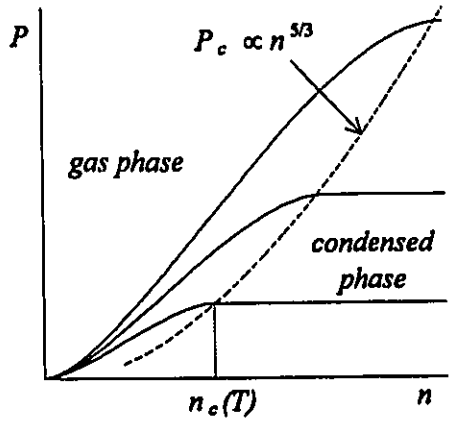

Fig. 2 Isotherms of an ideal Bose gas.

1.1.3 Properties of the condensate

Since not all the particles are in the ground state, the gas (or liquid in the case of superfluid He_4) has two components, a superfluid component formed by particles with ε_p=0, and a normal component formed by all the particles in the excited states ($\varepsilon_p \neq 0$). The normal component behaves as a classical gas or liquid, depending on the particle mass and density. The superfluid component, with velocity vector v, will have irrotational flow, expressed as

$$\nabla \times \mathbf{v} = 0 \tag{17}$$

This equation means that the condensate is moving as a whole. It is derived from the general principles of quantum mechanics, which postulate that since the particles are invariant under translation (a consequence of the macroscopic occupation of a single state), the condensate can be described by a single wave-function which is a product of all the condensed particle wave-functions.

The zero viscosity flow usually associated with superfluidity stems from the fact that the condensate is described by a single wave-function. Modification of this wave-function by the walls of a pipe or atoms of a lattice through which the condensate might be flowing would be highly improbable, since it would involve the simultaneous action on a macroscopic number of particles. Therefore, pipe walls and other obstacles cannot be a source of resistance since they do not "see" the condensate, or the condensate does not "see" them!

The only possible source of viscosity is the depletion of the condensate by the creation of quasi-particles. Quasi-particles (the particle aspect of the group of states is called a quasi-particle) can be created by the excitation of some of the condensed particles into low level excited states . As long as the number of particles still in the condensed state is much greater than one, a quasi-particle can be viewed as a distortion brought about by condensed particle pair interactions moving through the condensate.

By conservation of energy obstacles cannot create quasi-particles as long as the latter have a positive energy in the laboratory frame of reference. For a single quasi-particle, its energy in the lab frame is $\varepsilon_{qp}(k) + \hbar\mathbf{k}\cdot\mathbf{v}$, where $\mathbf{k}$ is the momentum of the quasi-particle, $\mathbf{v}$ is the velocity of the condensate and $\varepsilon_{qp}(k)$ the quasi-particle rest energy. Therefore if (note $v=|\mathbf{v}|$ and $k=|\mathbf{k}|$)

$$v > \text{minimum of } \frac{\varepsilon_{qp}(k)}{\hbar k} \tag{18}$$

momentum is being transferred from the condensate into quasi-particle modes, this is

analogous to the viscous damping of a flow where kinetic energy is being transferred to heat. Therefore, there is a maximum critical velocity

$$v_c = \min(\varepsilon_{qp}(k)/\hbar k) \tag{19}$$

at which a particle can move through the condensate (or that the condensate can move at) with zero viscosity. For low energy excitations at low temperatures, the phonon dispersion relation

$$\varepsilon_{qp} = \hbar v_s k \tag{20}$$

can be applied to the quasi-particles. Substituting Eq. (20) into Eq. (19) we find that the critical velocity is v_s, the velocity of sound in the medium. This is the case for an ideal weakly-interacting Bose gas. If the particles were non-interacting, the energy of the quasi-particles would be

$$\varepsilon_{qp} = \frac{\hbar^2 k^2}{2m} \tag{21}$$

where m is the mass of the condensate particles. Substituting Eq. (21) into Eq. (19), we find that the critical velocity is zero, since the minimum of $\hbar k/2m$ is zero; this means that an ideal Bose gas is unstable with respect to any movement. Therefore, in order to have formation of a stable condensate, which could be observed experimentally, the non-condensed bosons in question must have a small repulsive and/or attractive interaction term making the gas a nearly ideal gas. Fortunately, most real systems of particles do exhibit such interactions; one in particular, excitons in a semiconducting crystal, will be examined in detail in the following section in the hope of demonstrating BEC of a nearly ideal Bose gas.

1.2 Excitons and Condensation

1.2.1 Semiconductor energy band structures

Electrons in crystalline solids are confined to energy bands separated by forbidden gaps where there are no available energy levels. The energy bands are actually many energy levels very closely spaced so as to resemble a continuum of levels, and originate from the inter atomic coupling of atomic electron levels. The energy gaps simply arise from the periodicity of the crystal lattice. In a semiconductor or insulator, the highest filled (with electrons) energy band is called the valence band. The electrons in the valence band are bound to their parent atoms. The next higher energy band is called the conduction band and electrons in this band are free to move through the crystal. An electron normally in the valence band can be excited into the conduction band if the excitation energy is larger than the energy gap, E_{gap}, between the valence and conduction bands. The excited electron will leave behind an empty *hole* in the valence band, which can be viewed as a particle with a positive charge and therefore not bound to the positively charged atomic sites. Thus if an electric field is applied to the crystal, the electrons and holes are free to drift through the crystal (in opposite directions due to their charge) and contribute to an increase in the electrical conductivity of the crystal.

The size of the energy gap will determine many features of the material; if it is comparable to the average thermal energy of the electrons, the material will act as a conductor, since many electrons will always be in the conduction band due to thermal excitation. If the gap is very large, the material is an insulator, since it is nearly impossible for electrons to be excited into the conduction band by thermal excitations. Most semiconductors have energy gaps between these two extremes, with energies corresponding to the visible and infrared wavelengths.

The energy bands of a semiconductor are a function of the electron wavevector **k**. Most direct gap semiconductors have nearly parabolic conduction and valence bands as

shown in Fig. 3a for small wavevector **k**. The term "direct gap" arises from the fact that the minimum energy for a transition requires no change in electron momentum $\hbar\mathbf{k}$. Indirect gap materials on the other hand (Fig. 3b), do require a change in electron momentum (absorption or emission of a phonon) for the minimum energy transition.

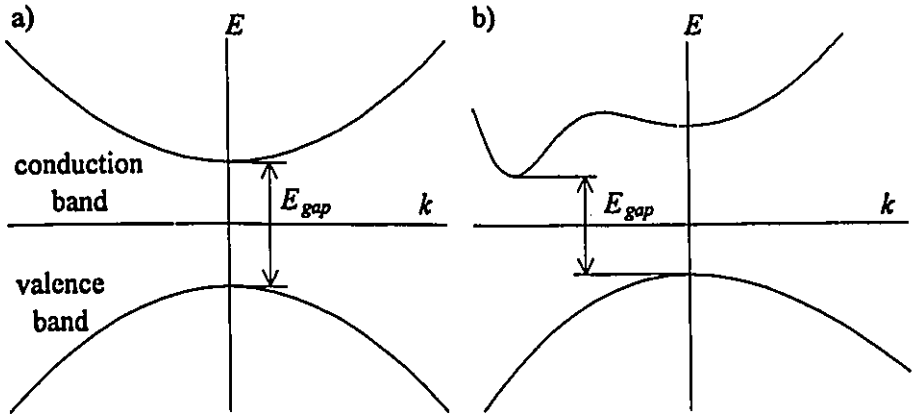

Fig. 3 Band structure for a) direct gap semiconductor, b) indirect gap.

The probability of a transition due to the absorption of a photon in the crystal will depend on the density of states of both the initial and final energy levels of the potentially excited electron. The density of states is itself related to the aforementioned band structure and the exact calculation of transition probabilities in semiconductor crystals is a very complex task. Experimentally, the probability can be represented by a single number which varies as a function of photon wavelength, the absorption coefficient α. The absorption coefficient for a particular crystal is determined by measuring the light intensity transmitted through the crystal as a function of wavelength, and by measuring the crystal thickness. The intensity of light which penetrates into a crystal as a function of distance is given by the Beer-Lambert law

$$I = I_o e^{-\alpha z} \tag{22}$$

where z is distance from the surface and I_o is the intensity of light incident at the surface. Substituting the crystal thickness into z, and the input and output intensities into I_o and I

respectively, α can be determined. However, there can be substantial uncertainties in the measured values of large absorption coefficients ($\alpha > 10^3$ cm^{-1}) since it is extremely difficult to obtain accurate measurements of I without using very thin crystals, which in turn are difficult to create and mount.

1.2.2 Effective Mass

In order to simplify the calculations for the transport of quantum particles such as electrons and holes through the periodic crystal lattice, the effective mass approximation is used. In the effective mass approximation, the quantum-mechanical motion of a free electron can be represented by an imaginary classical particle with charge e and effective mass m_e which responds to external forces in accordance with Newton's laws. The effective mass, m_e for electrons and m_h for holes in an isotropic medium is inversely proportional to the curvature of the energy band in which the particle resides.

$$\frac{\partial^2 E_c(k)}{\partial^2 k^2} = \hbar^2 / m_e \qquad -\frac{\partial^2 E_v(k)}{\partial^2 k^2} = \hbar^2 / m_h \tag{23}$$

The negative sign in the second equality corresponds to the positive charge of the hole. As can be seen in Eq. (23), the effective mass can be positive or negative, and range in size from any non-zero value to infinity, depending on the curvature of the energy band. An infinite effective mass (no band curvature) corresponds to an electron localized to a lattice site. In that case, the electron bound to the nucleus assumes the total mass of the crystal. A negative electron effective mass (a concave downward conduction band) means that the electron moves in the opposite direction to the applied force. For direct gap semiconductors near the band extrema (k=0), the electron and hole both have constant (as a function particle momentum $\hbar k$) positive effective masses due to the upwards parabolic conduction band $E_c(k)$, and the downwards parabolic valence band, $E_v(k)$.

1.2.3 Excitons

An electron excited into the conduction band is still physically close to the hole left behind in the valence band; and since they have opposite charge, they can bind together much in the same way a proton and electron combine to form a hydrogen atom, although in the present case, the Coulomb interaction is screened by the periodic lattice field. The electrically neutral entity formed by the bound electron-hole pair is called an exciton. It is a boson since the exciton spin is either 0 or 1; spin 1 excitons are labeled orthoexcitons and spin 0 excitons are called paraexcitons. The binding energy E_b, of the exciton follows the same type of series as observed in hydrogen, but is modified by the parameter ε, which takes into account the screening effect of the ions in the lattice.

$$E_b = \frac{e^4 \mu_{ex}}{2\hbar^2 \varepsilon^2 n^2} \quad n = 1,2,3,\ldots \tag{24}$$

where ε is the static dielectric constant and $\mu_{ex} = m_e m_h/(m_e + m_h)$ is the exciton reduced mass where m_e and m_h are the electron and hole effective masses respectively. Due to spin orbit coupling, the paraexciton will have a slightly larger binding energy than the orthoexciton. From Eq. (24), which is schematically represented in Fig. 4 (although the spacing between the exciton levels has been exaggerated for clarity), it can be seen that the exciton energies will be smaller than the energy gap of the crystal and will allow for

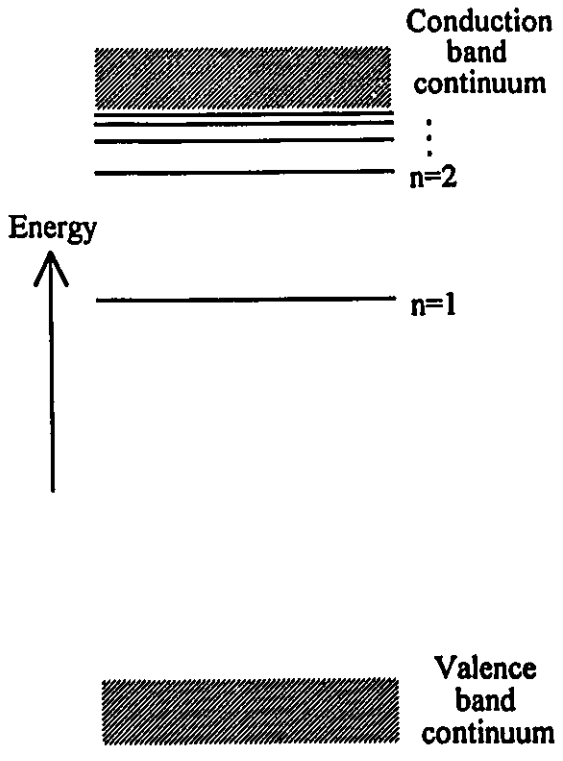

Fig. 4 Exciton energy levels for k=0.

absorption of photons in a region expected to be transparent to light. The exciton energy levels will manifest themselves as narrow absorption peaks in the crystal absorption spectrum.

The radius of the excitonic entity (the mean distance between the electron and hole) is given by

$$r_{ex} = a_o \frac{m_o}{\mu_{ex}} \varepsilon n^2 \qquad (25)$$

where a_o is the Bohr radius and m_o the electron rest mass. Small radius excitons for which r_{ex} is smaller or on the order of the lattice constant are usually bound to their parent atoms and are called Frenkel excitons. Larger radius excitons (r_{ex} > lattice constant), which we study in this work, are called Wannier excitons; this type of exciton can be viewed as a free particle, able to migrate through the crystal lattice until the electron recombines with a hole.

The time between exciton creation and recombination is the exciton lifetime τ, which is determined by the probability that the electron undergoes a transition back to the valence band either directly or indirectly. This probability is in turn governed by quantum selection rules and the density of the initial and final energy states. However, exciton recombination can be stimulated by thermal fluctuations or by the presence of an electric field which is of the same order of magnitude as the field between the electron and hole in the exciton.

Therefore in the diffusive regime a high purity crystal free of defects will allow excitons to travel the maximum theoretical distances, given by the diffusion length $\ell=(D\tau)^{1/2}$ where D is the diffusion coefficient. It is worthy to note that since the exciton is electrically neutral and has zero real mass, there is no charge or mass transport involved when the exciton diffuses across a crystal, only energy is transported.

The initial density of excitons optically created in a crystal will vary with depth and can be calculated in the following manner: the density of excitons in a layer of thickness dz

parallel to the illuminated face is equal to the loss of photons by absorption in the thickness dz divided by dz, assuming that every photon produces an exciton. Therefore, using Eq. (22) and the fact that the $I(z) \propto N(z)/A$ where $N(z)$ is the number of photons in a crystal at a distance z from the surface and A is the illuminated area, the density is given by

$$n(z) = -\frac{1}{A}\frac{d}{dz}N(z) = -\frac{1}{A}\frac{d}{dz}N_o e^{-\alpha z} = \frac{\alpha N_o}{A}e^{-\alpha z} \qquad (26)$$

where N_o is the incident number of photons at the surface and the absorption coefficient α is of the order of $3 \cdot 10^3$ cm^{-1} at λ=532 nm [6] (λ=532nm is the wavelength of the laser used in the following experiments). Note that for Eq. (26) to be valid, the time over which the photons are absorbed must be much shorter than the exciton lifetime. This is not a concern here since the laser pulse used in the experiments has a duration of 10 nsec, while the exciton lifetime in Cu_2O is 10 μsec [7]. From Eq. (26) it can be seen that the density of excitons at a given depth will directly depend on the incident number of photons since the absorption coefficient, illuminated area and pulse length are constants for the results presented in this work. It might be interesting in future experiments to vary the exciton density by changing the incident laser wavelength and hence the absorption coefficient since α for the exciton absorption lines in Cu_2O is well known, which is not the case for λ=532 nm.

1.2.4 Condensation of Excitons

BEC is believed to be the main cause of the spectacular properties of superfluid He_4 below the λ-point. However, due the large mass of the Helium atom, and large interactions between particles, the λ-transition has defied all theories attempting to explain it simply in terms of BEC. Therefore a more dilute variable density system where Bose statistical effects are predominant is needed to verify the quantum properties of the condensate.

Under the right conditions, excitons created in ultra-pure direct gap

semiconducting Cu_2O crystals are prime candidates to undergo Bose-Einstein Condensation. The excitons are bosons which behave very much like an ideal gas, due to their small mass, $2.7m_o$ [8] and small radius $r_{ex}\approx 0.7$ nm [9]. The criteria for a dilute gas, $nr_{ex}^3 \ll 1$ where n is the exciton density, is satisfied for excitons in Cu_2O for densities up to about 10^{20} cm^{-3} ($nr_{ex}^3 = 3\cdot 10^{-2}$). The small radius also helps prevent the breakdown of excitons into an electron-hole plasma at high density, called Mott dissociation. The Mott transition occurs when $nr_{ex}^3 \approx 0.3$ (in the case of Cu_2O; $n=10^{21}$ cm^{-3}). A repulsive exciton-exciton potential [10] insures against the formation of excitonic molecules such as biexcitons [11] which have been observed in CuCl [12], and provides stability for a moving exciton condensate as mentioned in section 1.1.3. Furthermore, the n=1 paraexciton is a forbidden transition in the quadrupole approximation and has an extremely large binding energy (≈150 meV). These two facts lead to an exceptionally long lifetime of about 10 μs, and stability against thermal dissociation since $k_BT \approx 0.5$ meV at 4K. However, since the n=1 paraexciton is a forbidden transition, the absorption coefficient is very weak ($\alpha \approx 3$ cm^{-1} [13]) and therefore paraexcitons must be created in an indirect fashion in Cu_2O: a photon with energy greater than E_{gap} excites an electron into the conduction band where it quickly (on the order of 10^{-12} sec [1]) relaxes to the bottom of the band by releasing phonons. The electron and hole combine to form an orthoexciton which has a very short lifetime, $\tau \approx 3$ nsec [7], after which it converts to the lower (12 meV) paraexciton state again by phonon emission.

The critical density required for BEC is calculated using Eq. (13); for paraexcitons (spin 0 and mass $2.7m_o$) at a temperature of 2K

$$n_c \cong 8\cdot 10^{16} cm^{-3} \tag{27}$$

which corresponds to a very dilute gas using the criteria mentioned above. To calculate the average density of excitons created by optical excitation in Cu_2O, Eq. (26) is used but the term $e^{-\alpha x}$ is replaced by the fraction of excitons absorbed (~0.63) within an absorption

length ($1/\alpha$). This average is akin to ignoring the low density contribution of excitons created deeper than an absorption length into the crystal and can be expressed as

$$n_{ex} = \frac{\text{photons absorbed} \cdot \alpha \cdot 0.63}{\text{area}} \tag{28}$$

Substituting into Eq (28), the number of photons in a laser pulse at near maximum power (for the Nd:YAG laser (λ=532 nm) used in the experiment), the illuminated area and the absorption coefficient for Cu_2O at λ=532 nm yields an average density given by

$$n_{ex} = \frac{8 \cdot 10^{14} \cdot 3 \cdot 10^{3} cm^{-1} \cdot 0.63}{3 \cdot 10^{-2} cm^{2}} = 5 \cdot 10^{19} cm^{-3} \tag{29}$$

Therefore the maximum average density (the exciton cloud will expand and the density will drop after the laser pulse) easily surpasses the critical density threshold at early times after the optical pulse ($t << \tau$) and the exciton gas can still be considered a dilute gas.

However, the theoretical density calculated in Eq. (27) assumed that the exciton gas is always at the lattice temperature, which is not quite true. Since the excitons in Cu_2O must be created indirectly, the initially excited electrons must shed excess kinetic energy by phonon production which results in heating of the exciton gas. Furthermore, at high density, an exciton can recombine producing a photon that is absorbed by another exciton (Auger process); this can further heat the gas and reduce its density. The overall heating effects at high densities (10^{18}-10^{19} cm^{-3}) can produce exciton gas temperatures in the 10K to nearly 90K range [14].

The lattice can also be heated by the phonons; the heating energy Q will be equal to the number of photons times the excess energy of the photons. This excess energy is given by E_{532}-$E_{n=1}$: the energy of the λ=532 nm photons (2.331 eV) minus the n=1 exciton energy (2.011 eV at 2K). The following expression can be used to evaluate the final lattice temperature in the volume delimited by the illuminated area and an absorption length. Eq. (30) will give the maximum possible temperature since it is assumed that no lattice energy diffuses away during the heating.

$$Q = m \cdot c(T) \cdot \Delta T$$
$$N_o \int dE = m \int_{T_o}^{T_f} c(T) dT \qquad (30)$$
$$n_{ex}(E_{532} - E_{n=1}) = \frac{\rho c_o}{4}[T_f^4 - T_o^4]$$

where $c(T)=c_oT^3$ (c_o=5.86·10^{-6} J/g·K) is the specific heat capacity at low temperature in Cu_2O [15], ρ=6.14 g/cm^3 is the mass density of Cu_2O, T_f and T_o=2K are the final and initial temperatures respectively. At exciton densities of 3·10^{20} cm^{-3} $T_f \approx$36K. The high exciton gas and lattice temperatures during and soon after the laser pulse, which increase with increasing exciton density, make forbidding conditions for condensation. However spectroscopic measurements have shown that the exciton gas and the excited volume of the lattice do reach thermal equilibrium with the bath temperature after approximately 30 nsec [4] and therefore condensation should occur some time after the pulse.

After creation, the packet of excitons will propagate away from the illuminated surface, initially accelerated by an enormous density gradient

$$\nabla n(z) = \frac{d}{dz} n(z) = \frac{-\alpha^2 N_o}{A} e^{-\alpha z} \qquad (31)$$

which is due to the large absorption coefficient. The gradient can be considered as one dimensional since the particles are spread out over a significant area (30%) of the sample face. If a condensate forms, it should travel drag free towards the opposite face at just under the speed of sound in Cu_2O, v_s=4.5·10^5 cm/s [1], and propagate as a coherent cloud of particles, since condensation is in momentum space and all the particles in the condensate have the same momentum. If the cloud of excitons does not condense, the particles will diffuse none the less towards the opposite face, but at reduced speed due to drag from interactions with the crystal lattice, and a Maxwell-Boltzmann broadening of the cloud should be apparent. In high quality samples with a thickness of a few millimeters, normal diffusive excitons will always reach the far side of the crystal since the diffusion length ℓ is of the order of 1 to 2 mm. Therefore the superfluid component will have to be distinguished from the normal, perhaps even quantum degenerate (but not

condensed), component by a change in the behaviour of the arriving cloud of excitons, such as the velocity or cloud size , at some critical density or temperature.

2 - Experiment

This section describes the steps followed in the preparation and execution of an experiment to find evidence for Bose-Einstein condensation of excitons in Cu_2O and provides details of the components used in the experimental setup.

2.1 Laser Beam Calibration

2.1.1 Temporal Profile

In order to attain the very high exciton densities required for BEC, a high intensity pulsed laser beam was used for optical excitation. The second harmonic of a Nd:YAG laser (λ=532 nm) with a maximum pulse repetition of 10 Hz was used for all the high intensity measurements. If required, the pulse rate could be lowered to 5, 2 or 1 Hz. The temporal shape of the pulse was verified with a 2 gigasamples/sec digitizing oscilloscope and a very fast photodiode (risetime≈falltime≈2 nsec). The results in Fig. 5 show an almost Gaussian pulse with a FWHM of about 10 nsec at maximum output power. At lower laser output power, the pulse has a much larger temporal width reaching the μsec range. For this reason the laser is always operated at full power with neutral density volume absorbing filters attenuating the beam. The asymmetry may be an artifact of the detector since the falltime may be slightly longer than the risetime, which is typical of photodiodes.

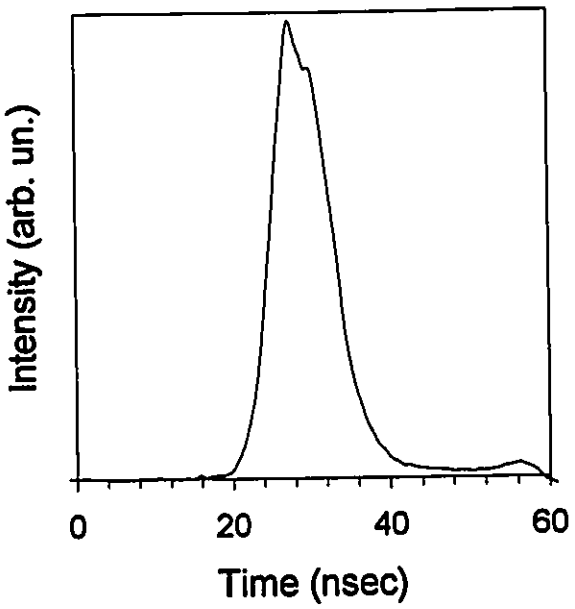

Fig. 5 Temporal profile of Nd:YAG laser beam.

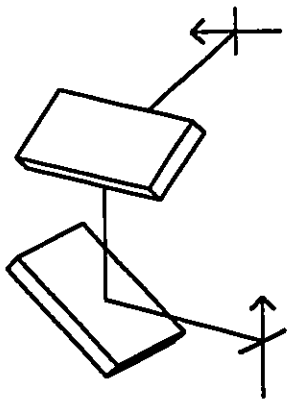

Fig. 6 Wang construction used to rotate laser beam by 90 degrees.

2.1.2 Spatial Profile

To verify the homogeneous spatial distribution of excitons in the plane parallel to the excitation surface, the profile of the laser beam was obtained using the same photodiode mentioned above, and a pinhole mask. A 400 μm diameter pinhole and the photodiode were both mounted on a translation stage which moved perpendicularly to the laser beam. This provided horizontal sampling of the beam profile. To vertically sample, the beam a Wang construction [16] (Fig. 6) was used; the two mirrors rotate the beam 90 degrees and the same translation stage can be used for a vertical profile measurement. Again the laser must be operated at maximum power to ensure the best possible beam profile, closest to the Gaussian shaped TEM_{00} mode.

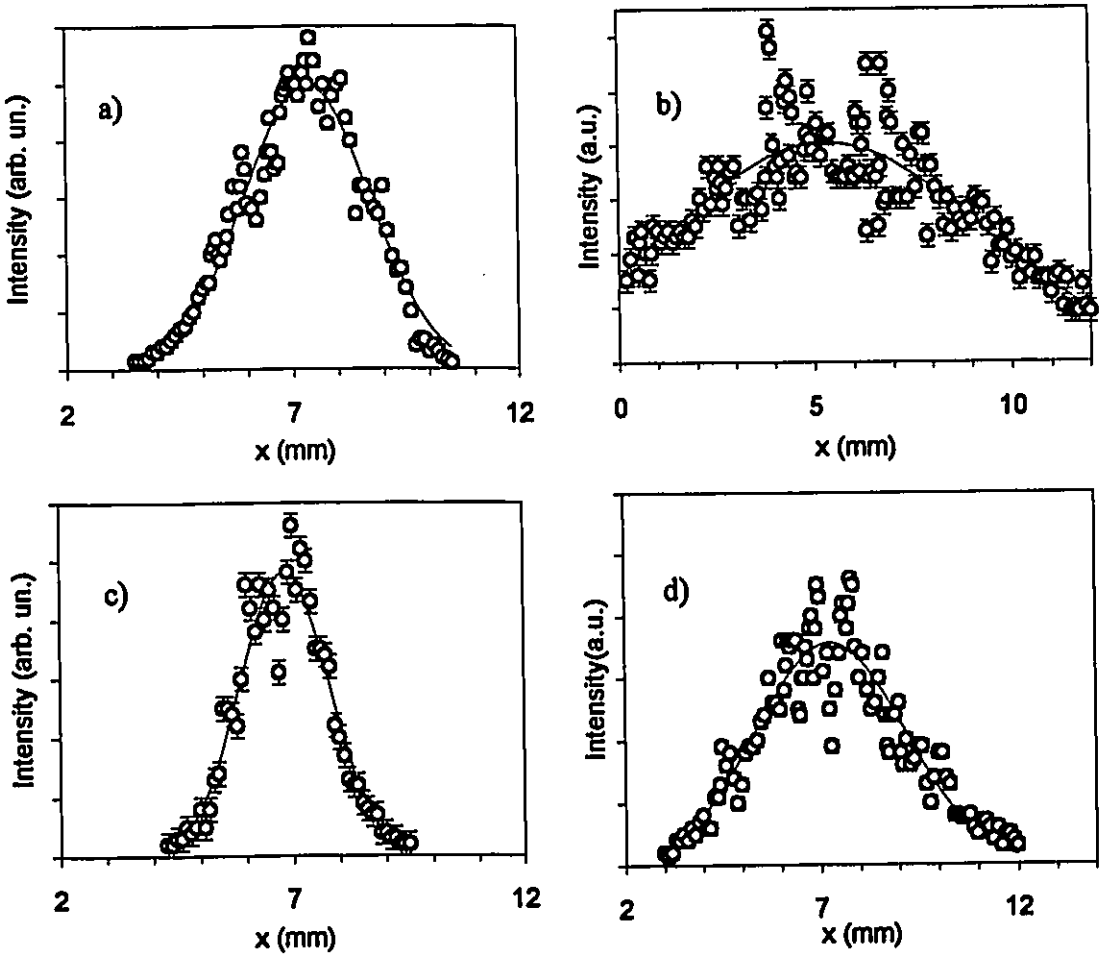

Fig. 7 Spatial profile of Nd:YAG laser beam at distance z. Horizontal profiles a) at z=5 m and b) at z=20 m. Vertical profiles c) at z=5 m and d) at z=20 m.

The results of these measurements are shown in Fig. 7 along with a best fit Gaussian profile. The beam width ($w(z)$: half width at $1/e^2$ of maximum intensity) in the horizontal plane is 2.5 mm at a distance of z=5 m, and w=8 mm at z=20 m. The beam width is slightly smaller in the vertical plane (w(5 m)=2 mm, w(20 m)=4 mm), indicating that the beam is not quite in the TEM_{00} mode.

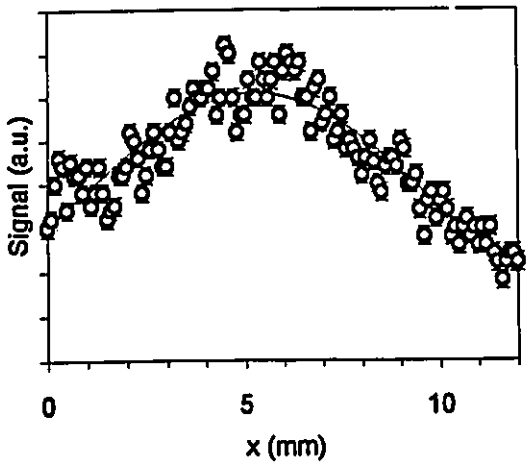

Fig. 8 Horizontal spatial profile of Nd:YAG laser beam at a distance of 20 m.

The intensity spikes or "hot spots" seen near the peak of the beam in Fig. 7 are undesirable since they can heat the sample locally and damage the surface even though the total power is at a safe level that would not burn the sample. Furthermore, the hot spots can falsify the exciton density estimates and smear out possible transitions in the exciton behaviour. The laser was recollimated to eliminate the hot spots and to maximize the output power, and the new beam profile was measured again as shown in Fig. 8. The beam quality has improved significantly (compare with Fig. 7b) and was deemed acceptable even though some small spikes were still present.

While performing the beam profile measurements a pulse to pulse variation of 5% to 10% in the intensity and a 1 nsec jitter in the pulse arrival time was observed. Unfortunately, the jitter in intensity and time is intrinsic to the laser. Such a jitter in intensity could also possibly smear out a transition in the results since a measurement near the transition may jump across and the standard averaging technique would record both sides of the transition. Over longer periods (~5 min.), the maximum drift of the total power was less than 5%. The total power of the laser beam measured with a power meter was 1.5 W at 10 Hz. The power of the beam passing through a 2 mm diameter aperture

mounted at a distance of 5 m from the laser optical port was 50±1 mW (at 10 Hz). This is the number used as the base for all other intensity and density calculations.

2.2 Exciton Detector

2.2.1 Exciton Mediated Photovoltaic Effect

Previous attempts at detecting the paraexcitons in Cu_2O using photoluminescence techniques [1, 2, 3, 4, 5], have not clearly demonstrated the phase change from a quantum degenerate gas to a condensate [17]. The principal reason is that the paraexciton luminescence is extremely weak due the optically forbidden paraexciton transition; therefore the luminescence must be sampled near the excitation spot soon after (t<40 nsec) the laser pulse, when, and where the signal is strong. However, the conditions in the exciton gas at early times, as mentioned earlier, are not conducive to the formation of a condensate: the effective temperature of the exciton gas is still much higher than the lattice temperature since the excitons were created with excess kinetic energy and must shed this energy by emitting phonons. Furthermore the exciton cloud is in a highly non-equilibrium state with an enormous density gradient pulling the excitons away from the surface and rapidly expanding the cloud. If there was formation of a condensate, it could be far from the initial excitation spot where the exciton gas temperature reaches equilibrium with the lattice and where there is a more uniform density distribution of particles above the critical density.

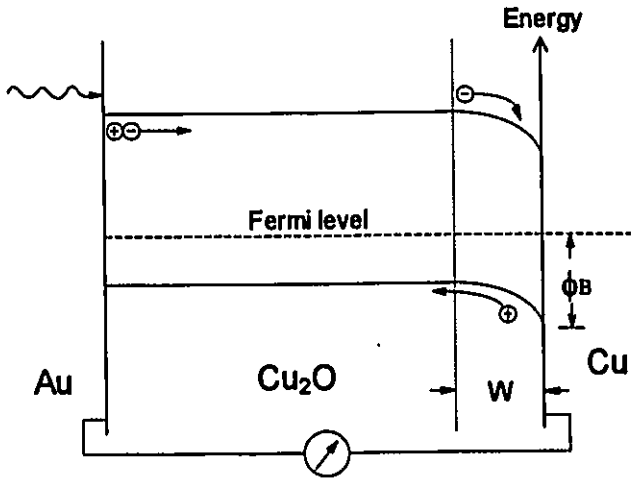

Fig. 9 Sample arrangement for low intensity measurements. Neutral, bound electron-hole pairs (excitons) optically created near the Au electrode diffuse to the Cu/Cu_2O interface where they are dissociated by the local field and collected as free electrons and holes.

A different method of detecting the excitons, far from the excitation surface and at much later times (t >>pulse length) when the exciton gas temperature is at equilibrium with the lattice and bath, was required. The method used in this work is the exciton mediated photovoltaic effect [18]. Figure 9 demonstrates the basic idea behind this method. The Cu_2O sample (a p-type semiconductor) is sandwiched between a semi-transparent Au electrode on the left and a Cu electrode on the right. Au provides an ohmic contact for Cu_2O. An ohmic contact can pass very large currents with only a small voltage drop across the metal-semiconductor junction. The Cu contact on the other hand is a rectifying contact: at the Cu/Cu_2O interface the respective Fermi energy levels line up and lead to a bending of the energy bands of the semiconductor. The potential barrier, ϕ_B at the interface is of the order of 1 volt [19, 20]. This results in a high electric field region W (where W is the depletion width) in the Cu_2O crystal which extends to a depth of 10-100 nm [21]. The local static electric field will thus have a magnitude of $\phi_B/W \cong 10^5$-10^6 V/cm. The field required to dissociate an exciton in Cu_2O is of the order $E_b/r_{exc}e \cong 10^6$ V/cm. Therefore a fraction of the excitons reaching the Cu/Cu_2O interface will be dissociated and detected as an external current (photocurrent) or voltage (photovoltage) between the Au and Cu electrodes. The two circuits used for measuring the photovoltage or photocurrent are shown in Fig. 10, although for the time resolved measurements the photocurrent mode was used since the time constant in the photovoltage mode is very long due to the high sample resistance.

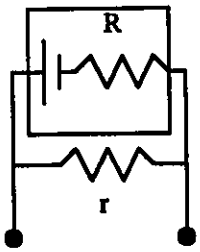

Photovoltage: r>>R

Photocurrent: r<<R

Fig. 10 Circuits used to measure the photo signal.

2.2.2 Low Intensity Spectra

To measure the photovoltaic response of the Cu_2O sample as a function of wavelength at low intensities (10^{-5} W/cm^2) and to probe the exciton behaviour at very low densities, the optical setup in Fig. 11 was prepared. The image of the lamp filament is

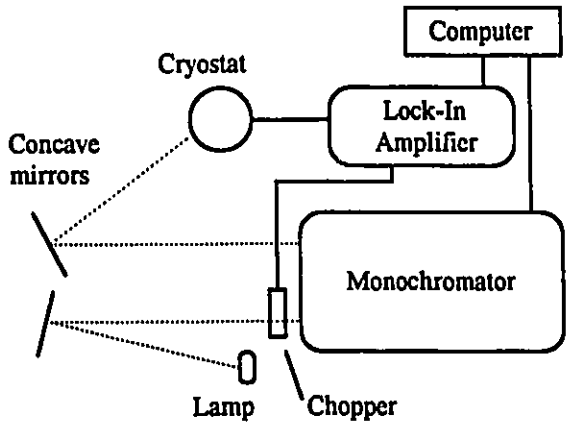

Fig. 11 Optical setup for measuring low intensity photovoltaic spectra.

focused on the entrance slit of the monochromator with a concave mirror. The output beam is again focused onto the sample which is in a vacuum in the cryostat. Under computer control the monochromator scans a range of wavelengths at a predetermined step size. At each step the computer reads the photovoltage from a lock-in amplifier. The lock-in amplifier is a precision instrument which reads very small AC voltages at a reference frequency and phase set by a light chopper, which is also modulating the input beam at the same frequency.

The spectra shown in Fig. 12 reveal the photovoltaic signal produced by illuminating the Au side of two very different types of Cu_2O samples. In case a) the sample is a very thin 35 μm Cu_2O layer grown on a Cu substrate held at T=77K. Case b) is for a 2 mm thick natural growth high quality Cu_2O single crystal at T=2K; this is the type of sample used in the rest of this work. The photosignal observed in both cases is due to field stimulated exciton dissociation in the depletion layer (i.e. exciton mediated photovoltaic effect). However, in case a), excitons are created directly in or near the depletion layer and the signal amplitude varies with the absorption coefficient. The large drop in photosignal at approximately 575 nm reveals the yellow band edge; superimposed are the n=2, 3 and 4 yellow exciton absorption peaks. In case b) the excitons are created near the Au face as unbound electron-hole pairs relax into the n=1 paraexciton within a few psec [22]. The process is nearly independent of excitation wavelength for energies greater than E_{gap} (red edge) since all the electrons and holes relax to the bottom (top for holes) of their respective energy band (Fig 3) before diffusing any significant distance. The long lived paraexcitons can then diffuse to the opposite crystal face where they are

dissociated at the Cu/Cu_2O interface and measured as a photocurrent. Hence the signal in thick crystals depends only on the diffusion coefficient D and not on the absorption coefficient. An exception here is the quadrupole absorption line of the n=1 orthoexciton, which can only be observed at very low temperatures in high quality samples. Due to the extremely low absorption coefficient for the quadrupole line, excitons are again being created directly in the depletion layer. Computer simulations [18] show that spectra like that of Fig. 12b) which have very low wavelength dependence of the photocurrent at energies above the gap, imply very long diffusion lengths of $\ell \approx 1$ mm.

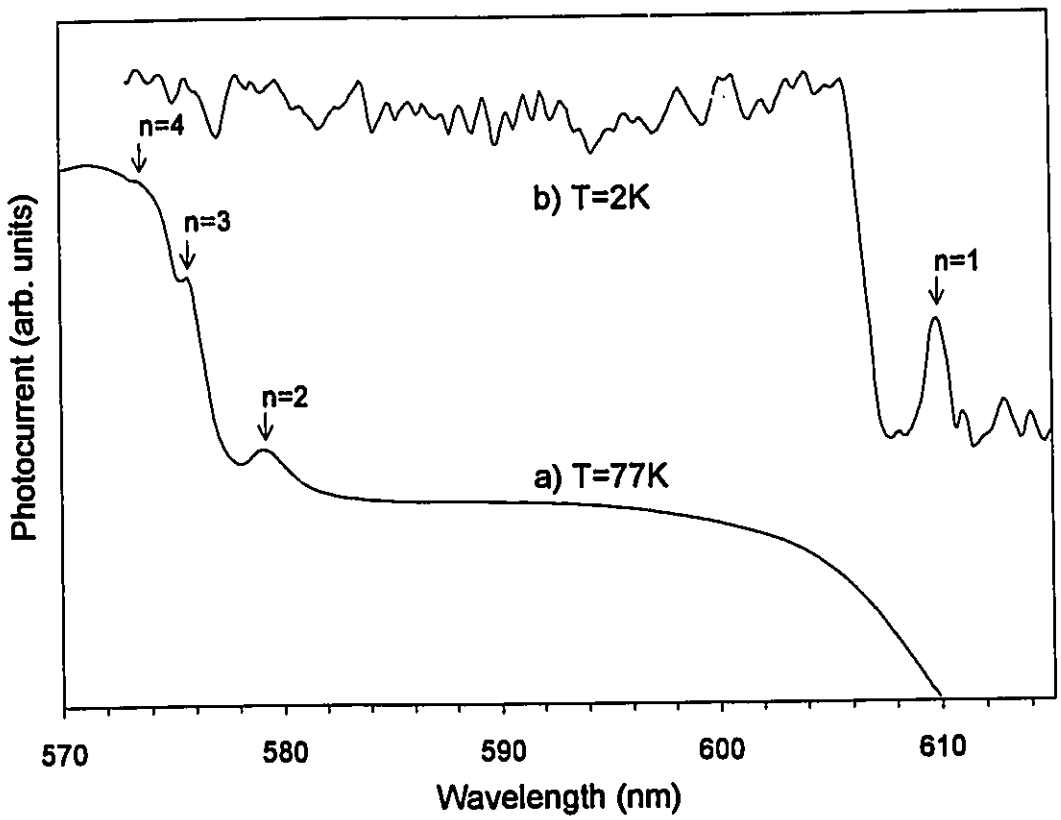

Fig. 12 Photocurrent spectra of Cu_2O samples arranged as in Fig. 9. a) Thermally grown sample, thickness 35 μm, T=77K; b) Natural growth single crystal, thickness 2mm, T=2K.

2.2.3 High Intensity Excitation

For multimegawatt/cm^2 pulsed illumination and time resolved measurements needed for Bose-Einstein condensation and exciton transport studies, the sandwich

electrode arrangement of Fig. 9 is unsuitable. Firstly, the high intensity laser beam would damage the semi-transparent Au electrode. Secondly, the extremely high series impedance of the thick (a few millimeters) Cu_2O sample at low temperatures (~10^{12} Ω) together with various distributed capacities would result in relatively high time constants for the detected

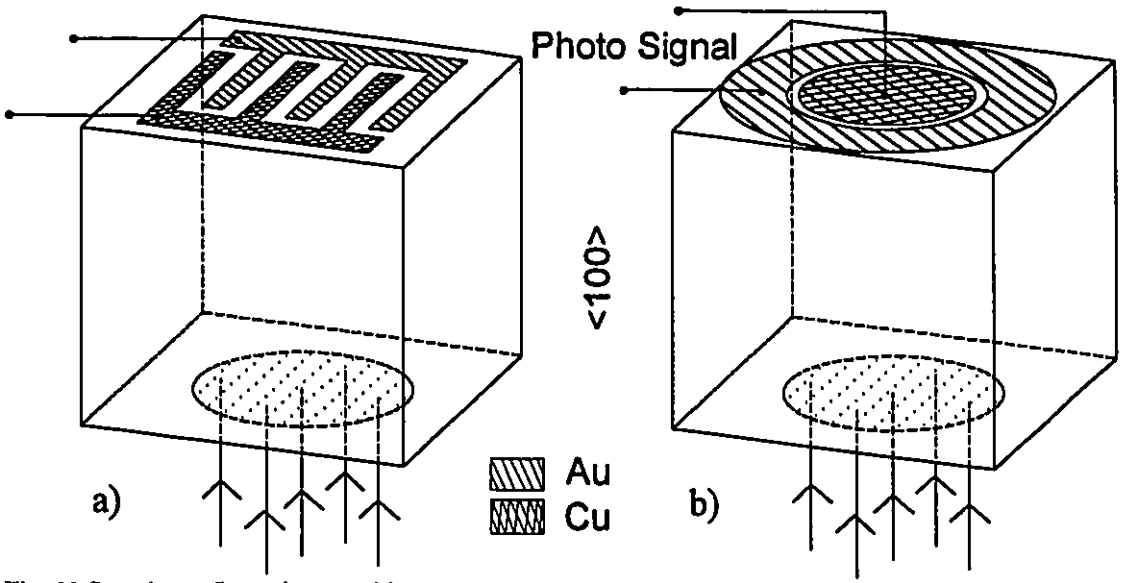

Fig. 13 Sample configurations used in high intensity measurements.

signal, preventing the nanosecond resolution required for the time-resolved experiment. Thus all the time-resolved high intensity studies were made with one of the arrangements shown in Fig. 13 where the Au electrode (single cross-hatch) is deposited on the same face as the Cu electrode (double cross-hatch), opposite the illuminated area as depicted by the dotted circle on the bottom of the crystal.

The active detector region is the 10-100 nm thick volume of Cu_2O under the thin 50 nm Cu film (double cross-hatch) deposited on the top sample face. The total detector area is the same in both cases a) and b), about 3 mm^2. However the circular electrode in case b) produced, on average, higher signal amplitudes than the "finger" electrodes in case a). This is because the active area in the center of the face, where the excitons are expected to arrive, is twice as large in case b) as compared to case a).

The detector resistance between the Au and Cu electrodes will be approximately the same in both circle and finger configurations. This can be shown by calculating the ratio of resistances per unit z (a_z is perpendicular to the electrode face) using Schirapelli's formula for dielectric materials

$$R_{unit\ z}^{circle} / R_{unit\ z}^{line} = \frac{\ln(1 + d_1 / r)}{2\pi} \Big/ \frac{d_2}{L} \tag{32}$$

where r is the radius of the circle, d_1 is the spacing between the circle and ring, L is the total length of all the lines and d_2 is the spacing between the lines. Substituting the values r=1 mm, d_1=0.125 mm, L=12 mm and d_2=0.254 mm, the ratio in Eq. (32) gives a value of 0.86. The value for L was obtained by summing the five finger edges (5 × 2 mm) and adding the three ends (3 × 0.75 mm).

The capacitance of the Schottky barrier will also be similar in both configurations since it is proportional to the detector area and is approximately

$$C \cong \varepsilon A / W \tag{33}$$

where ε is the dielectric constant, A is the area and W is the depletion width.

2.2.4 Detector Efficiency

The efficiency of the Schottky barrier exciton detector was determined by comparing the absolute optical power delivered to the sample by the monochromator to the absolute electrical power output by the sample. At λ=532 nm and at T=77K, efficiencies of the order of 0.1% have been measured for thin samples of the type shown in Figs. 9 and 12a. This is in agreement with values obtained by Berezin and Weichman for above gap illumination [23]. For thicker samples (such as Figs. 12b and 13) we have measured efficiencies of the order of 0.01% at low intensity. The overall efficiency of the process at high intensities including surface recombination and two-body Auger recombination (where one exciton recombines producing a photon which heats another exciton) in thick crystals is difficult to evaluate quantitatively; we have estimated it to be

of the order of 0.0001%. However it could vary by an order of magnitude from sample to sample due to crystal quality and surface preparation before electrode deposition. But this would only affect the signal amplitude for a given experiment without undue influence on the time resolved results or observed critical behaviour.

2.3 Sample Preparation

Since preparation of the samples required polishing and chemical etching the thickness of the sample varied from experiment to experiment. Sample 1 had a thickness of 3.56 mm to 2.2 mm and sample 2 had a thickness of 3.74 mm to 2.7 mm. Both samples were approximately 4 mm x 4 mm square. Sample 3 was substantially larger, 11 mm x 10 mm x 8.3 mm but had a defect compromising its quality as shown in Fig. 14. All three crystals were oriented such that the <100> face was perpendicular to the largest face on which the electrodes were deposited.

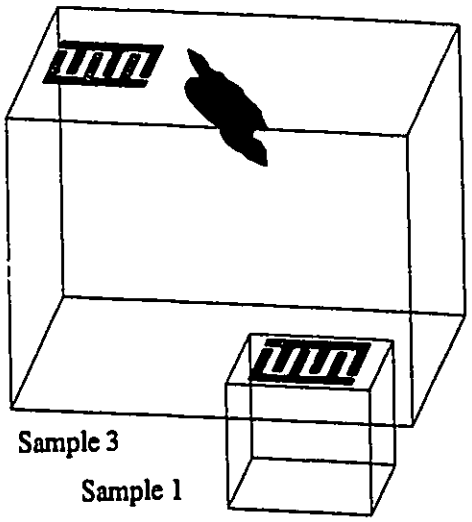

Fig. 14 Comparative sizes of samples 1 and 3.

2.3.1 Polishing

The first step in preparation of the samples was the polishing. Polishing is performed to remove any scratches or previously damaged electrodes on the surface of the crystal. If large scratches are not removed they will be further enlarged and deepened by the chemical etch performed afterwards, since the etching rate is not isotropic. The following polishing recipe produces good results, however the times shown (per face) can vary substantially if the preceding step is not thoroughly completed.

Table 1 : Polishing procedure

Step	Operation
1	9.5 μm Al_2O_3 powder on glass sheet with distilled water for ~5 min. Rinse with distilled water/methanol solution in ultrasonic cleaner. Wipe dry with tissue paper. N.B. This step removes by far the most amount of material from the crystal.
2	6 μm Diamond compound (Metadi II) on Ravel cloth with Metadi fluid which is a type of polishing fluid for ~15 min. Rinse with distilled water/methanol solution in ultrasonic cleaner. Touch dry with tissue paper.
3	0 to 1 μm Diamond powder on Microcloth OR 1 μm Diamond compound on Texmet with distilled water for ~10 min. Rinse with distilled water/methanol solution in ultrasonic cleaner. Wipe dry with optical tissue paper.
4	0.05 μm Al_2O_3 powder on Microcloth with distilled water for ~5 min. or until satisfied with surface quality. Rinse with distilled water/methanol solution in ultrasonic cleaner. Touch dry carefully with optical tissue paper.

The final three steps are performed on a adjustable speed turntable. All the polishing was done without any type of special holder. It is very important to clean the sample, hands and tweezers before every step to avoid contamination of a finer powder with a coarser one. Note that it is a good idea to stop every few minutes to rinse, dry and observe the sample through a microscope to see if it is time to proceed to the next step. Knowing when to change powders is more an art than a science, but by using a microscope one can tell when the scratches and dimples in the surface are as small as

possible, and further polishing yields little visible change on the surface. Only two crystal faces per sample were fine polished, the two faces perpendicular to the <100> direction; the other four surfaces were stopped at step 2 since the larger scratches were removed and no excitons important to the experiment would be near these surfaces. When finished, all the surfaces were highly reflective and flat. Minor craters (<1 μm) remained but these seemed intrinsic to all the crystals since if the small craters were polished away, others were uncovered somewhere else on the surface.

2.3.2 Chemical Etching

Chemical etching was performed on the sample to eliminate the top layers which may have been damaged during polishing. In addition the electrodes deposited afterwards could easily be scratched off by the wire contacts if no etching was performed. The following recipe developed by solar cell researchers has been found to lower the surface recombination rate and maximize the barrier field at the Cu/Cu_2O interface [24].

Table 2: Etching procedure

Step	Operation
1	Rinse in distilled water.
2	Soak for 1 min. in methanol with final 20 sec in ultrasonic cleaner.
3	Etch for 3 min. in HBF_4 (~5 μm/min), then dilute quickly with distilled water so that there are no spots etched more than others.
4	Repeat steps 1 to 3 if electrodes are still present from a previous experiment.
5	Repeat step 1.
6	Repeat step 2.
7	Soak for 90 sec in Bromine(2% vol.)/Methanol solution with final 30 sec in ultrasonic cleaner.

8	Repeat step 2.
9	Repeat step 7.
10	Repeat step 2.
11	Repeat step 2 again.
12	Rinse in distilled water.
13	Quickly blow dry with He or N_2 to eliminate water spots.

2.3.3 Electrode Deposition

To dissociate the excitons into electron hole pairs injected into an external circuit and measure a photovoltage, Au and Cu electrodes were deposited on the polished face of the crystal. Since the crystals are very small (for human manipulation), and the electrodes even more so, special consideration of the design of the evaporation mask had to be taken into account to correctly deposit the electrodes without overlapping them and causing a short circuit.

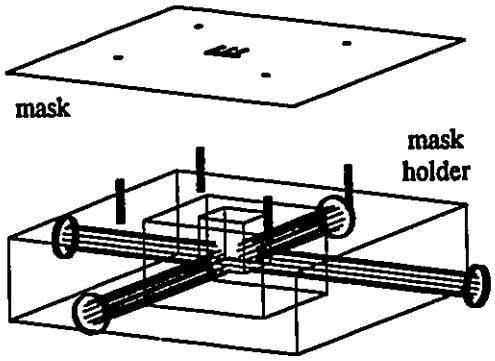

Fig. 15 Mask (finger type) and mask holder for electrode deposition.

The finger pattern mask shown in Fig. 15 was made by laser lithography at NRC and the circular pattern mask (Fig. 16) was made in the Physics machine shop. Both masks are designed to consistently deposit two different materials within 250 μm or less of each other, on an area less than 4 mm by 4 mm square. The four guide posts embedded in the mask holder also shown in Fig. 15 are placed so that when the finger pattern mask is rotated 180°, the second electrode interlocks with the first electrode. The procedure to deposit the finger pattern electrodes is as follows: the crystal is placed in the center of the holder and held by Teflon screws. The edges of the crystal are then lined up with two

marks on the mask to position the crystal exactly. Also the surface of the crystal is aligned to be flush with the surface of the holder so that there is a minimum of space between the mask and the crystal. This ensures that even if the sample is not exactly over the source of the evaporator, the electrode will not shift due to the angle. The first evaporation using Au is carried out and the mask holder is removed from the evaporator. The mask is removed and replaced rotated 180°; this must be done carefully so as to not move the sample and ruin the alignment. The sample is once again placed into the evaporator and the Cu electrode is evaporated. Both the Au and Cu electrodes were evaporated to about the same thickness, 40 to 50 nm. The order in which the materials are evaporated is important: evaporating Au then Cu reduces the exposure of the Cu/Cu_2O interface to heat, which chemically reduces to form a non-conducting layer of CuO between them, which in turn reduces the barrier height and efficiency of the exciton detector.

The same procedure is followed for the circular electrodes except that three

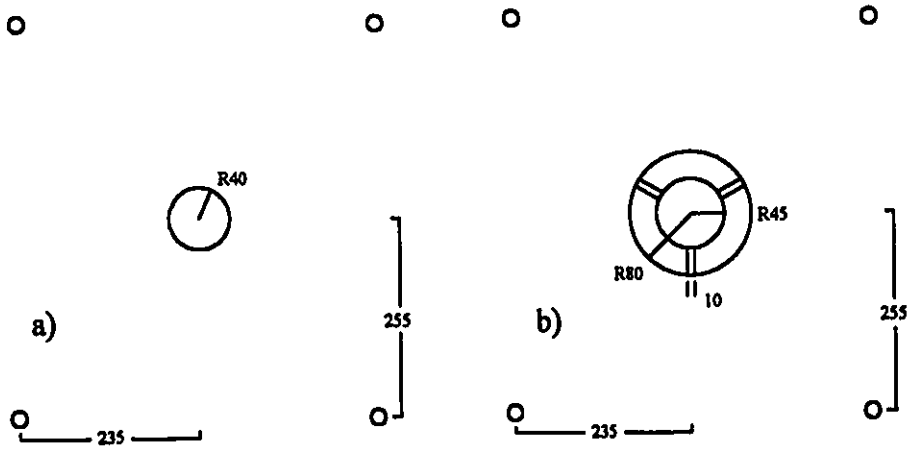

Fig. 16 Masks used for circular electrode evaporations. a) Cu electrode, b) Au electrode. The four outer holes match the posts on the mask holder. Dimensions are thousands of an inch.

evaporations are performed. The outer Au ring is deposited first, then the mask is rotated 180° and a second Au ring is deposited over the first. The second evaporation has the effect of covering the blind spots produced by the three symmetrical center supports and

producing a complete ring. Note that for the second evaporation a circular mask with a radius slightly larger than the circular center section of the mask in Fig. 16b) is placed over the center section to nullify any misalignment. The final evaporation of the center spot using Cu is performed with the mask in Fig 16a) in place.

Sample 3 was a much larger crystal, so it would seem logical that bigger electrodes could be deposited to gather more signal. But it had a large defect inside as shown in Fig. 14, slightly offset from the center. The defect is an excellent recombination area for excitons, and so only a portion the crystal could be used. Since this sample could only be used for a short time before being returned to its owner (before the circular electrodes were developed), only the finger electrodes were deposited.

2.3.4 Wire Contacts

The most difficult part of the sample preparation was making a good bond between small gauge Au wires (referred to as contacts) and the electrodes. The bond must be able to withstand an extreme change in temperature (from 300 K to 2 K) and hence differential thermal contraction. Several attempts were made with Silverprint, a type of conductive paint used for printed circuits, but after a few thermal cycles, the bond became very brittle and was likely to fail. Two different two-part epoxies, Epo-Tek 20E and Epo-Tek 20G, were tested. The 20E easily survived many thermal cycles. However this type of epoxy must be cured at 200°C for 5 minutes, and in this short time a substantial layer of CuO forms between the Cu/Cu_2O interface, greatly reducing the detector efficiency. Furthermore the bond is so strong that a part of the crystal can be broken off when attempting to remove the epoxy. The Epo-Tek 20G cures at room temperature but could not withstand the low temperature stresses and has never survived a thermal cycle. Currently the most promising fastener is called Circuitworks, a compound similar to Silverprint, manufactured for the same purpose, but with a thicker consistency when applied and not as brittle once dry.

There are two methods for bonding the contacts to the electrodes. A small chunk of fastener (epoxy/Silverprint/Circuitworks) is deposited on the electrode and the contact is smeared into the small chunk of fastener, then held in place until the fastener is dry. Alternatively, a small chunk of fastener is deposited on the end of the wire and the wire is carefully dropped into place onto the electrode. For greater success the end of the wire should be bent to make a small foot, enlarging the effective contact area. Beware when applying Silverprint to control the flow of the liquid since it naturally spreads out over the sample surface, and can easily short the Au and Cu electrodes.

To remove contacts made with the Epo-Tek 20G epoxy, Silverprint or Circuitworks compound, methanol was used to dissolve and lift the contact. However the Au electrode is also easily removed with the methanol. The Cu electrode requires etching and/or polishing for complete removal since the Cu atoms actually diffuse into the crystal.

Mechanical contacts have been successful with sample 3, but the area of the bus (the bar connecting the electrode fingers) was four times larger than normal (as shown in Fig. 13a). Samples 1 and 2 were too small for such an arrangement. Furthermore mechanical contacts are inherently noisier (electrically) and were found to be less reliable than the bonded contacts.

2.3.5 Sample Holder

The first generation sample holder shown in Fig. 17a) was fabricated from Delray, a black plastic, to electrically insulate the sample. On one side of the holder an approximately 4 mm square by 2 mm deep hole was machined to hold the sample. In this hole another cylinder 3 mm in diameter by 2 mm deep was drilled to allow for a large cross-section of helium gas or liquid to be in contact with the sample. Next a 2 mm diameter hole was drilled straight through for the laser beam. The smallest diameter hole selects only the center of the beam, so that the variation of the intensity as a function of radius is on average 30% (from Figs. 6a and 6c) when the sample is at a distance of 5 m

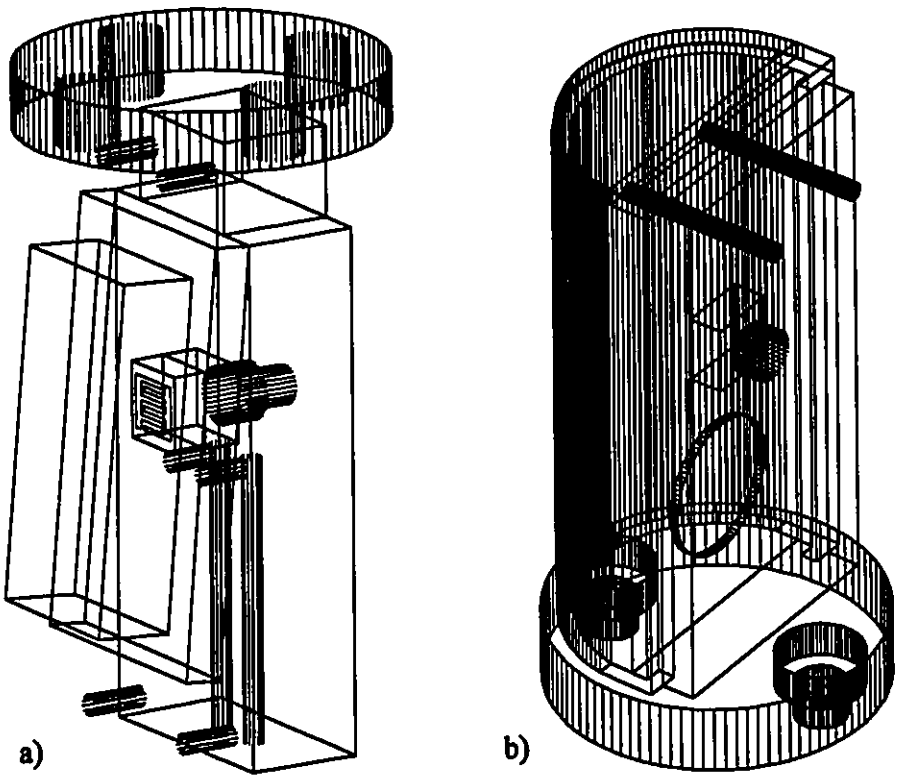

Fig. 17 a) 1st generation sample holder made from Delray plastic, b) 2nd generation sample holder made from Cu.

from the laser optical port.

A rectangular light cap was made to prevent stray light from hitting the electrodes directly. The "front cell" photovoltaic signal generated by the parasitic light coming through the cracks between the light cap and sample holder was useful in determining the time zero reference point. However, under certain conditions, stray light hitting the electrodes could, for an unknown reason, totally disable the detector. Therefore the second generation sample holder shown in Fig 17b) improved the light cap design so that no parasitic light was able to reach the electrodes. Several other design improvements were made, such as reversing the order of the 2 mm and 3 mm diameter holes for better access to the sample face for non-normal laser beam incidence (such as in a double beam experiment), and a provision for mounting a temperature sensor inside the light cap. It was also soon apparent that the two channels funnelling He to the sample inside the light

cap were not cooling the sample sufficiently when operating in He gas, and so the second sample holder was fabricated from Cu, one of the best thermal conductors at low temperature. The sample was not electrically insulated in the Cu sample holder, but this did not affect the results or increase the noise in the measurements since the sample resistance at low temperature is of the order of $10^9\ \Omega$.

The Au wire contacts leading from the sample were soldered to posts at the bottom of the sample holder where two larger conventional wires were also soldered to provide connections to a coaxial cable. Since the light cap on the second generation sample holder enclosed the entire back surface, the conventional wires are soldered to the same posts protruding on the opposite side of the sample holder from Au wires. These posts are vacuum feedthroughs which are insulated from the holder body.

2.4 Experimental Setup

2.4.1 Single Beam Excitation

In this experiment single optical pulses were used to create an exciton gas in the Cu_2O sample. The photovoltaic signal resulting from excitons dissociated at the opposite sample face was measured as a function of time and averaged over many pulses, typically 100 to 200 pulses. Since the distance traveled by the excitons is fixed (the sample thickness) the arrival time of the signal reveals the exciton velocity. Figure 18 shows a schematic of the experimental setup, the laser light (dashed line) is directed onto the

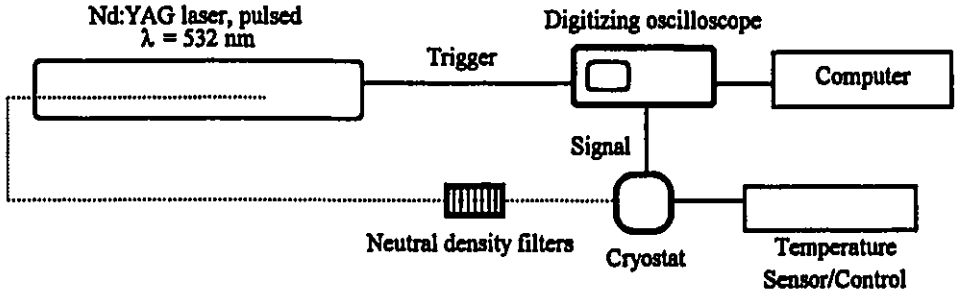

Fig. 18 Experimental setup for time resolved high intensity single beam pulsed laser measurements.

sample (not shown for clarity) in the cryostat. High reflectivity (≈99.9%) multi-layer dielectric mirrors must be used to direct the laser beam due to the extremely high beam intensities (10^7 W/cm^2).

Several volume absorbing neutral density filters are placed in the beam path to control the incident intensity on the sample surface. The filter order is important, low density filters must be placed before the higher density filters, since a high density filter could absorb too much light and suffer permanent damage. The filter set was mounted as close to the cryostat window as possible (while leaving room to align the beam on the holder aperture) to minimize any displacement or deviation of the beam by the filters.

The sample holder was screwed to a mounting plate attached to a long stainless steel rod. Along the rod ran a doubly shielded coaxial cable which was soldered to the posts on the holder as mentioned earlier. This rod was lowered into the cryostat and positioned so that the laser beam directly entered the 2 mm aperture normal to the sample surface.

The trigger is an electrical pulse emitted by the laser power supply to warn the measurement device (in this case a digitizing oscilloscope) to start the data acquisition. But as mentioned earlier a better time zero reference is the front cell signal, although, once calibrated, the front cell signal was not necessary. The electrical trigger was 122 nsec ahead of the optical trigger with the sample 5 m from the laser optical port. This value reflects an inherent delay of the optical pulse (built into the laser), the different length of cable for the trigger and signal pulses, and the time for the light to travel the optical path. The delay value would change slightly if the cryostat was moved, but most of the results obtained were at this distance.

The digitizing oscilloscope, a Tektronics model 620 (maximum sampling rate 2 gigasamples/sec with 500 MHz bandwidth), made the experiment possible by being able to average a trace hundreds of times at 500 megasamples/sec and reduce the background noise which can be of the order of a few millivolts (as compared to signals of a few

millivolts in amplitude) at such high sampling rates. The full sampling rate was not used since the oscilloscope memory could only hold 2000 points per trace and a 4 μsec window was required for the experiment. Once the waveform was averaged sufficiently, a computer with a GPIB interface could download the curve from the oscilloscope to a file on hard disk. A special computer program was written to do this automatically.

To extract accurate information from the waveforms, some substantial post-processing was required. Firstly, a noise background was subtracted from the waveform to eliminate noise structures which did not change significantly during the acquisition time and therefore were not averaged out. Often many different backgrounds were used for different traces due to the changes in the noise signature over several minutes. A background is acquired under the same experimental conditions except that the laser beam is blocked from reaching the sample. The waveforms were then time shifted to the correct time zero found with the optical trigger. Then a moving window average (the value of a point is the average value of m/2 points before and after the point where m is the adjustable window size) was performed to further reduce noise and increase the accuracy of the following analysis. The size of the window is determined by the width of the peak being smoothed and the signal to noise ratio; the larger the window, the more noise will be eliminated. However too large a window will distort the true underlying signal by widening the peak and reducing the amplitude. The analysis is then performed; a computer reads the waveforms into memory and a program determines the peak amplitude, peak arrival time, peak width (FWHM), peak half width on the leading edge (HWHM), the total integrated signal and the fixed window integrated signal (integrated signal over a fixed time interval). The results are output in an ASCII format, readable by spreadsheet and graphing programs. The program, developed by the author, which performed the data transfer and the analysis is over 40 pages long and will not be presented here.

Temperature readings were supplied by two sensors, one below and one above the

sample. The sensors are silicon diodes which have a temperature calibrated resistance. The temperature controller sends small electrical pulses (which also add noise) to the sensor and determines the resistance which is then converted to a digital temperature reading. The upper sensor was closer to the sample and deemed more correct although accuracy was limited by temperature gradients in the gas and liquid phases. To reach temperatures below 4.2K, the helium liquid enters the bottom of the cryostat sample chamber and is pumped out of the top, flowing by the sample. The liquid can be converted to He gas by heating it slightly at the bottom of the chamber. The sample temperature is controlled by the pumping speed, the amount of He liquid being let into the chamber and two heaters mounted below and above the sample. The temperature gradients are induced by the effect of pumping and the small heaters. When the liquid He is pumped fast enough, it enters the superfluid phase at T=2.17K. At this temperature there is a sudden change in the appearance of the liquid; the bubbles which permeated the He liquid all disappear due to the enormous heat conductivity of the superfluid. A significant amount of sample heating can be induced by the laser at high intensity for experiments performed in the He gas; this is not as much a problem in the superfluid phase since the superfluid thermal conductivity is 10^6 times larger. When operating in the gas the pulse repetition rate was therefore lowered at the highest intensities in order for the heat to be carried away between pulses.

The initial measurements on sample 1 were plagued by high frequency noise commencing at the trigger point and lasting for over 1 μsec. It could not be entirely averaged out even for very long integration's (1000 pulses), and subtracting a background spectrum did not significantly help since the noise structures (electrical ringing) were slowly changing.

Even with all the noise present, there was a large structure approximately 1 μsec after the trigger. The anomalous signal in Fig. 19 is interesting because for a distance corresponding to the crystal thickness of 3.56 mm, and a velocity corresponding to the

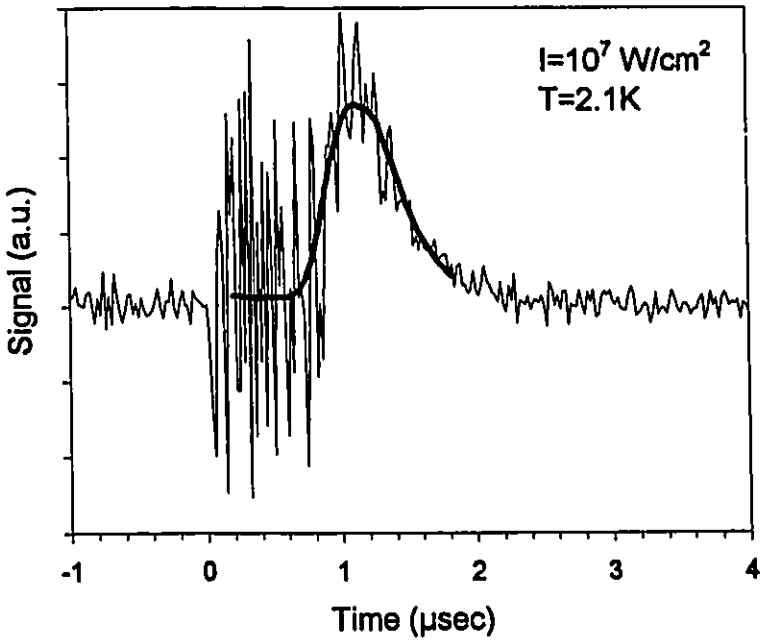

Fig. 19 Preliminary measurements using sample 1 with thickness 3.56 mm.

sound velocity in Cu_2O, v_s=4.5×10^5 cm/s, excitons would be expected to arrive at the electrodes at about t=0.8 μsec (from $t=d/v_s$). However the time zero is uncertain since the front cell signal is lost in the noise and, as mentioned above, the trigger is not necessarily the true zero. The noise would have to be reduced at the source.

Determining the source of the noise was simple; when the Pockels cell (a high voltage power supply for the laser flashlamp) was turned off, the noise disappeared. But eliminating the noise proved to be much more challenging since the Pockels cell was required for high intensity laser output.

To reduce the noise solid metal plates were placed directly between the laser power supply and cryostat, and a Faraday cage was installed around the cryostat sample chamber, both to no avail. After extensive testing, it was determined that the noise was permeating all the conducting components in the room. Since it was impossible to shield the Pockels cell without redesigning the laser and laser power supply, all the other components of the experiment had to be shielded in order to reduce the noise. As mentioned earlier, the cable leading down into the cryostat to the sample was a doubly

shielded coax, and the coaxial cable from the cryostat to the oscilloscope was covered in a aluminum braided sleeve. And finally, what turned out to be the most critical shielding, was a piece of crumpled aluminum foil wrapped around the outside top casing of the stainless steel rod going down into the cryostat and also including the coax connections for the temperature sensor cable and the signal cable. The noise was reduced by a factor of about 100 with the temperature sensor disconnected, and by a factor of about 25 with the sensor connected. The factor of roughly four in the noise is due the fact that the temperature controller was receiving and transmitting the noise through the temperature sensor cable and could not be shielded without causing incorrect readings.

2.4.2 Double Beam Excitation

The purpose of the double beam experiments was to observe the interaction between two packets of excitons simultaneously moving through the crystal. The single pulse from the Nd:YAG laser is split into two beams using a 50%/50% beamsplitter as shown in Fig. 20. One beam is directly aligned on the sample as in the single pulse excitation experiment, the other beam is reflected back and forth several times before reaching the sample surface at an angle less than 2 degrees from the normal. The longer optical path of the second pulse introduces a time delay δt between the pulses. During the time delay the exciton cloud from the first pulse moves away from the illuminated surface,

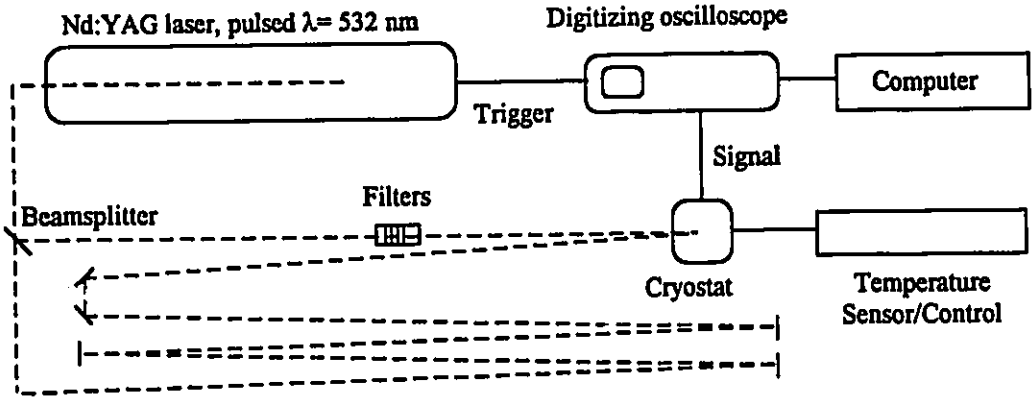

Fig. 20 Experimental setup for time resolved high intensity double beam pulsed laser measurements.

and therefore the distance between the two exciton packets can be controlled by changing the optical path of the second beam. The intensity of the second beam is reduced by the beam divergence and so it is refocused with a lens to the same diameter, at the sample surface, as the first beam. Two independent sets of filters control the beam intensities. The temperature control of the sample and the acquisition and analysis of the data were performed in the same manner as explained above. All the double beam experiment results were obtained with sample 1 using the first generation sample holder at the lowest attainable temperature, 2.1K.

3 - Results and Analysis

This section will describe and interpret the results of many successive experiments designed to uncover the presence of an exciton Bose condensate in Cu_2O. Two different types of experiments will attempt to reveal the superfluid character of the exciton gas, and the quantum interference effects produced between two condensates.

3.1 Single Pulse Excitation

3.1.1 Diffusive Transport

The results in section 2.2.2 showed that excitons created at low density in steady state on one side of a Cu_2O crystal diffuse across the crystal within an exciton lifetime. But no direct information on the speed or spread of the excitonic particles is obtained from these measurements. On the other hand the time resolved measurements in the pulsed regime presented in this section, do reveal such information on the excitons diffusing through the crystal. Figure 21 shows the photo signal (solid line) resulting from the diffusion of excitons created with the pulsed Nd:YAG laser at λ=532 nm. The three

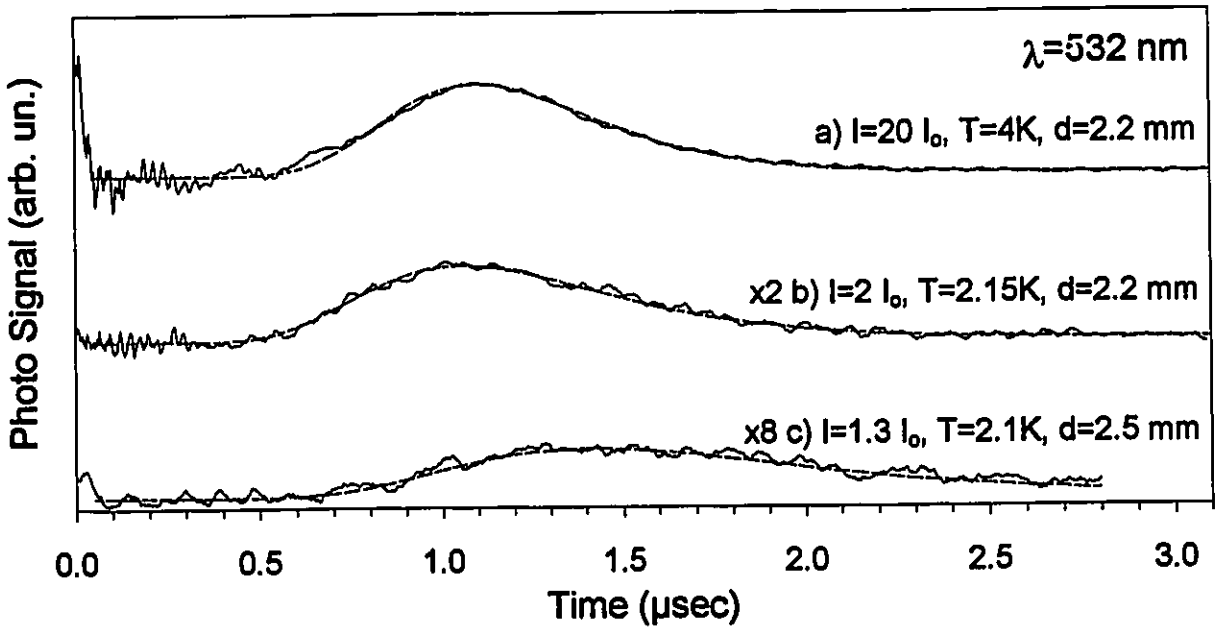

Fig. 21 Experimental curves fitted (dashed line) with a diffusion equation. Traces b) and c) are vertically expanded by a factor of 2 and 8 respectively. I_o corresponds to a laser intensity of 10^5 W/cm^2.

traces were obtained under different conditions as labeled on the figure, but all in the same crystal, sample 1; therefore, no change in the diffusion constant due to sample quality should be observed. The results were well fitted (dashed line) by a diffusion equation [25] of the type

$$n(z,t) = (4\pi Dt)^{-3/2} e^{-t/\tau} e^{-z^2/4Dt} \qquad (32)$$

where D is the diffusion constant and τ is the exciton lifetime (10 μsec). The cloud is assumed to travel through the crystal at constant speed v, and the variable z in Eq. (32) is replaced by $v \cdot t$. Therefore there are two fitting parameters D and v; τ does not significantly alter the shape of the curve since the detection time is much smaller than τ. For trace a) at T=4K, $D \cong 1400$ cm^2/s and $v=0.4v_s$; for traces b) and c) at $T \cong 2.1$K, $D \cong 2000$ cm^2/s, $v=0.39v_s$ for case b) and $0.32v_s$ for case c). These values are high when compared to those reported in the literature [25, 26], indicating that sample 1 is of very high quality. Furthermore the ratio of the diffusion constants at the two temperatures is in accordance with the deformation-potential scattering theory [27] extended to excitons [28] which predicts that D is proportional to $T^{-1/2}$. The basic idea of this theory is that the scattering time of an electron traveling through the vibrating lattice is related to the static "deformation potential" of the conduction band.

3.1.2 Ballistic Transport

The preliminary results obtained using sample 1 (d=3.56 mm) were extremely encouraging, once most of the noise was eliminated. A fast rising photo signal with a maximum at 0.8 μsec and totally unlike the diffusive results above, is clearly evident in Fig. 22, in contrast with noisy signal in Fig. 19. The signal is due to a cloud of excitons traveling at nearly the speed of sound in the crystal, since v=3.56 mm/0.8 μsec=$4.45 \cdot 10^5$ cm/s. The incident intensity that produced this exciton packet was $100I_o$ where $I_o=10^5$ W/cm^2 and the crystal temperature was 2.1K for this trace. In the current configuration an intensity of $1I_o$ corresponds to $6.5 \cdot 10^{13}$ photons in each pulse. Using Eq. (28), the incident

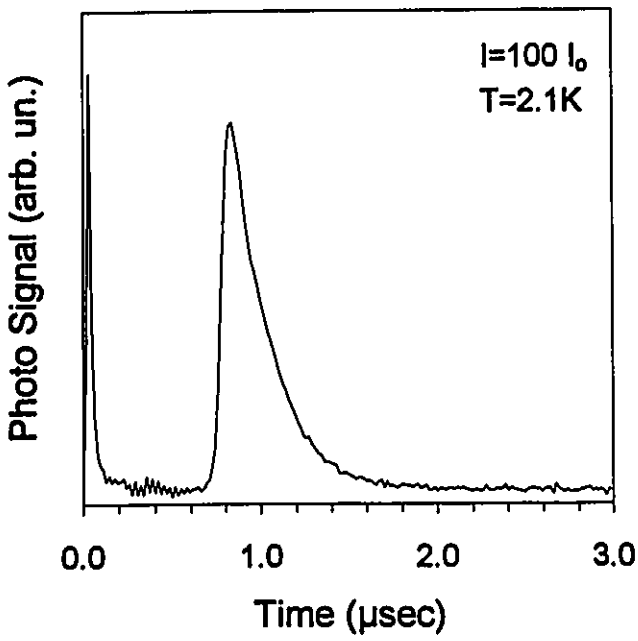

Fig. 22 Photo signal obtained with a sample of thickness d=3.56 mm. The incident laser wavelength was 532 nm.

intensity can be converted to an average initial density of $6.5 \cdot 10^{15}$ photons x 0.67 x 0.65 / $9.5 \cdot 10^{-6}$ cm^3 = $3 \cdot 10^{20}$ cm^{-3} for this case. The extra factor of 0.65 takes into account the reflections at the cryostat double quartz windows (index of refraction≈1.7) and at the sample surface (index of refraction≈2.7). The density of the exciton packet near the front surface in this case is well above the critical density at T=2.1K. The "prompt" photo signal near t=0 is from the laser pulse itself; it is visible since the light cap on the first generation sample holder was not entirely light tight and allowed some scattered laser light to directly illuminate the "finger" type electrodes. This "prompt" photo signal is not due to migrating excitons, it is from optically excited free carriers being created in the Cu/Cu_2O interface which are then immediately swept across the potential barrier to create a photo signal.

In the preceding analysis the cloud of excitons generated at high intensity was assumed to be moving at constant speed after a rapid initial acceleration. To verify this assumption, the time resolved photo signal was measured in a thicker sample where the excitons had to migrate a much larger distance in order to be recorded. Figure 23 shows a trace obtained in sample 3 at high intensity ($125I_o$) and low temperature (2.1K). It is similar to the shape of the trace in Fig. 22, although the packet arrives at a much later time since the sample thickness is d=8.3 mm. The velocity can be calculated as before (8.3 mm / 1.85 μsec) and gives about $4.5 \cdot 10^5$ cm/s which is again close to v_s. Therefore the packet does travel with constant velocity through the crystal over macroscopic distances.

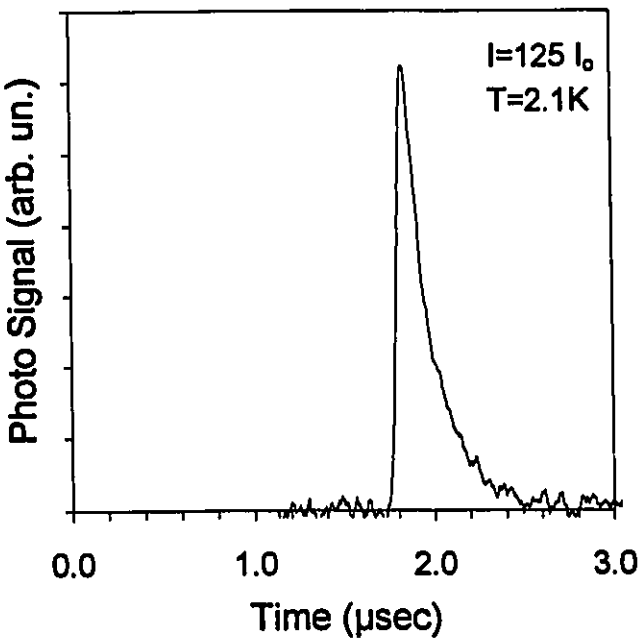

Fig. 23 Photo signal obtained with a sample of thickness d=8.3 mm.

Furthermore the packet in Fig. 23 has the same temporal width as the high intensity trace shown Fig 22. Therefore the cloud of excitons is traveling through the crystal as a group with little velocity dispersion. This implies that the temporal width of the photo signal reveals the spatial size of the packet.

As further evidence of the packet's constant velocity and negligible dispersion when migrating through the crystal, a compilation of the results obtained at many different thicknesses in three different samples are shown in Fig. 24. All the results were obtained at T=2.1K and at high intensities (>50I_o) above the critical intensity (discussed in section 3.1.4) where the velocity and packet size are relatively unaffected by changes in intensity and small changes in temperature. The velocity of the packet maximum v normalized to v_s is plotted against the sample thickness, and is nearly constant over 6 mm (Fig 24a). The packet size, calculated by multiplying the HWHM (on the front edge) times 2, times the packet velocity, is also plotted in Fig. 24b as a function of sample thickness. Again the packet size remains nearly constant for all the distances.

It is understood that the exciton cloud starts as a compact entity a few μm thick, its size determined by the absorption coefficient. However a large expansion must take place during and/or shortly after the laser pulse as can be inferred from Fig. 24, since the packet remains a nearly constant 350-400 μm in size for the duration of the voyage across the sample. Such rapid expansion of the cloud has been numerically simulated for the case of excitons in Cu_2O [29]. The slight variations in the packet size can be attributed to

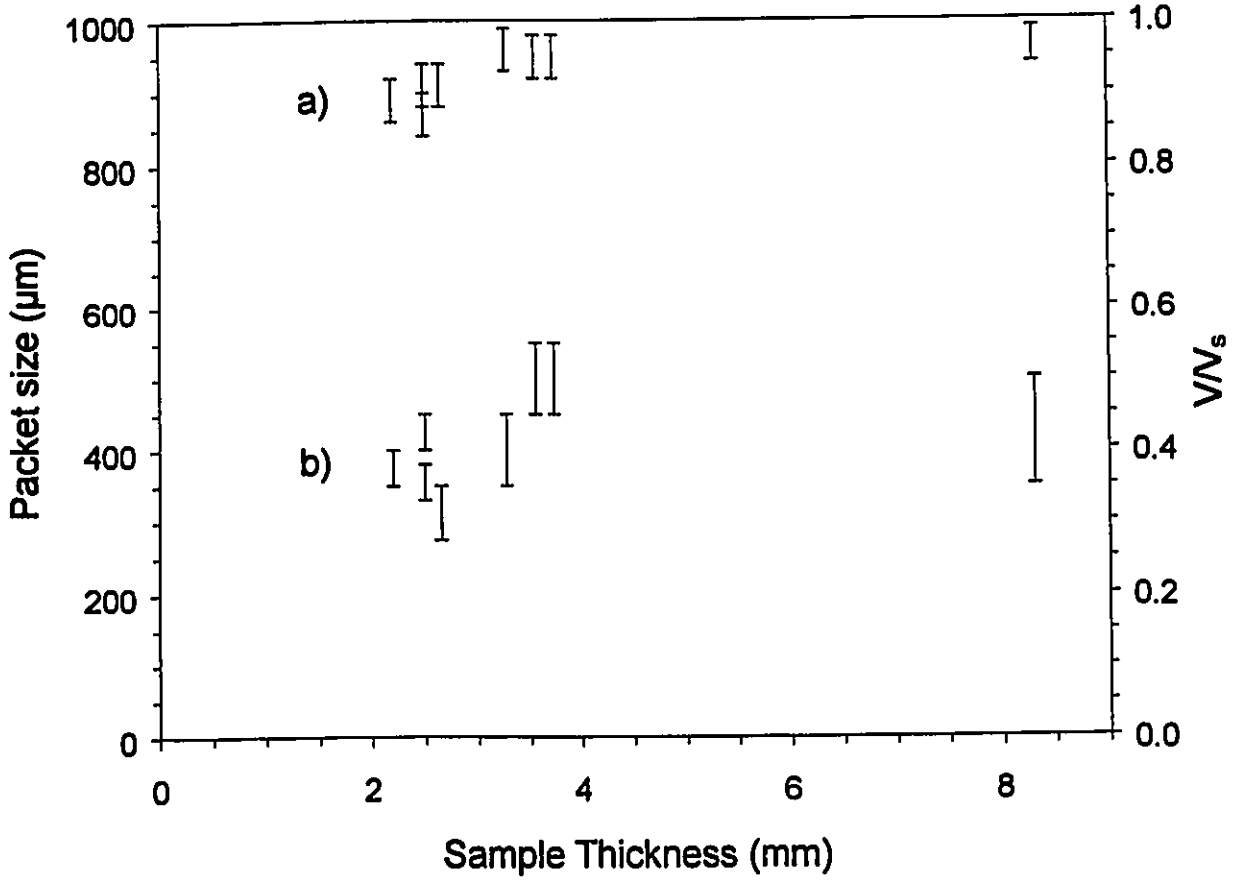

Fig. 24 a) Normalized speed of exciton packet, b) Size of exciton packet from HWHMx2 times speed of packet for different sample thickness (bottom).

different diffusion coefficients in the 3 samples, which are of different quality. The diffusion coefficient would affect the initial rate of expansion.

The HWHMx2 on the front edge is used instead of the FWHM to determine the size of the packet because of the asymmetrical shape of some of the curves. The asymmetrical shape is believed to be an artifact of the detector. Nearly symmetrical packets are obtained when the electrodes are fully insulated against parasitic light, and therefore, the fall time of the detector may be affected by stray light. This hypothesis is supported by preliminary experiments with longer wavelength excitation, where the absorption length is on the order of 100 μm. The results, not shown here, indicate asymmetrically delayed photo signals at high excitation intensities even with the second generation sample holder which fully shields the electrodes from stray light. The laser

light in this case is penetrating directly through the sample and onto the electrodes from within the sample.

3.1.3 Excitonic Transport as a Function of n and T

More measurements, performed at different incident intensities at a fixed temperature of T=2.1K, are shown in Fig. 25 for a sample crystal of thickness d=3.56 mm. The temperature was the lowest attainable temperature in the superfluid He. As the laser intensity is reduced, the delayed photo signal decreases in amplitude, as expected, since the amplitude is related to the exciton density measured at the Cu/Cu_2O interface. The signal maximum shifts to later times at lower intensities, signifying slower exciton transit

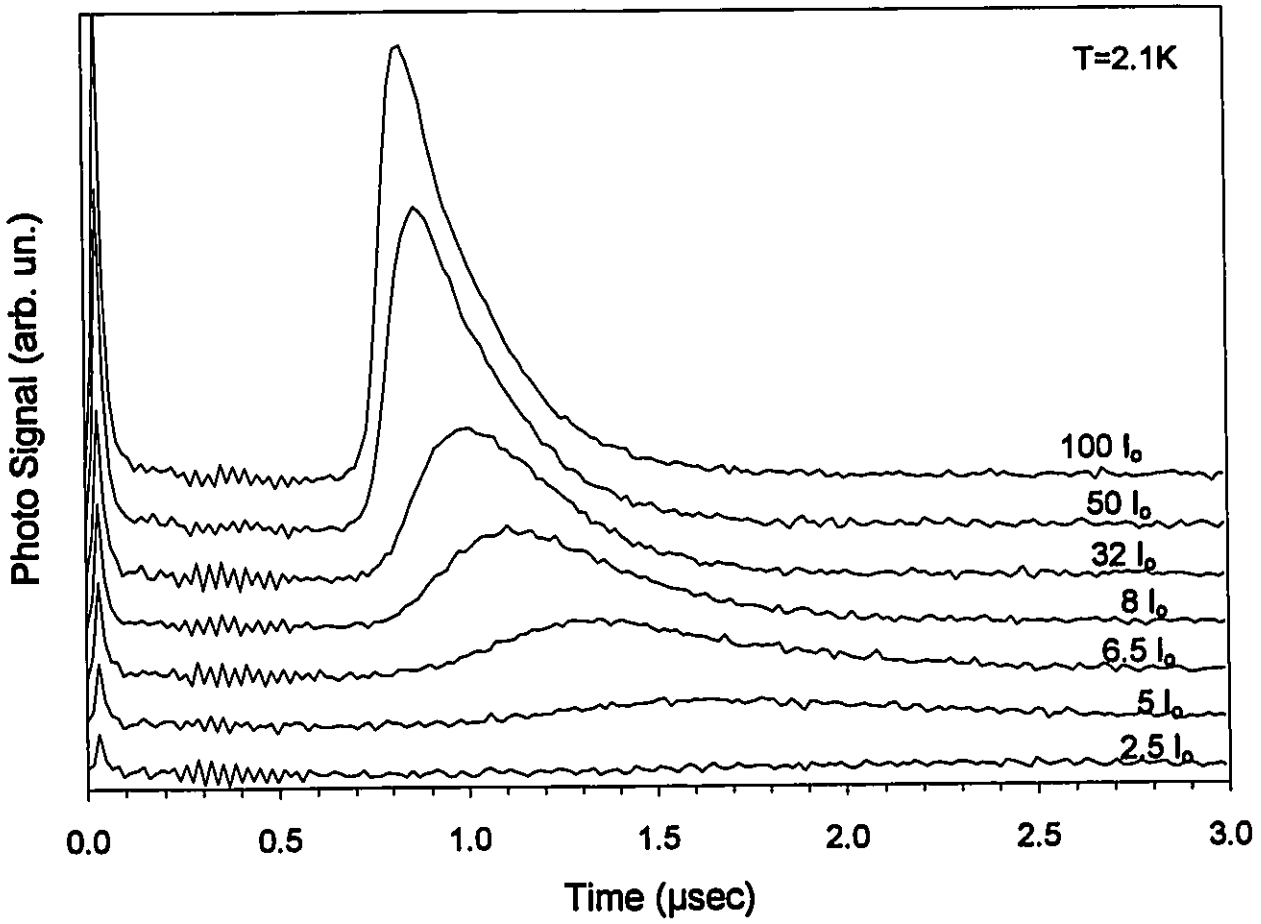

Fig. 25 Photo signal obtained with a sample of thickness d=3.56 mm for various laser intensities at a fixed temperature of T=2.1K.

times; therefore the exciton transit velocity is related to the initial exciton density gradient, as expected. However at higher intensities the peak velocity saturates near the speed of sound as calculated in section 3.1.2. The temporal width of the photo signal also undergoes large changes as a function of intensity i.e. density. The exciton cloud shows a wide spatial distribution of particles at low intensity as predicted by the diffusion model. However, as the intensity is raised, the cloud reduces in size and saturates at a minimum size, even though the excitons are moving at a greater speed and could diffuse farther from the center of the cloud, according to the standard diffusive model.

The measurements presented in Fig. 26 are the results of an experiment performed at T=2.1K, as above, except that sample 2 (d=3.7 mm) was used. Also, instead of using Silverprint to bond the wire contacts to the "finger" type electrodes, the H20E epoxy was used. As mentioned in section 2.3.4, the epoxy must be heated to be cured, and in the process the barrier height, and hence collection efficiency of the detector is reduced. The signal amplitudes measured in this experimental run were an order of magnitude lower than in the previous case at comparable incident intensities. There are two reasons for the lower signals: a reduction in detector collection efficiency and a lower sample quality. The lower sample quality of sample 2 can be attested by comparison to measurements made with sample 1, also prepared with the H20E epoxy, which gave higher signal amplitudes under the same conditions. However the said results (shown in Fig. 26) still had lower amplitudes than the measurements obtained in sample 1 with Silverprint contacts, confirming that the collection efficiency is affected by the curing process. The qualitative behaviour of the signal in Fig. 26 as a function of intensity, such as the saturation of the velocity at high intensity, and the broadening of the distribution at low intensity, is the same as in Fig. 25. This demonstrates that the general behaviour of the results is not greatly affected by the detector collection efficiency or individual sample quality.

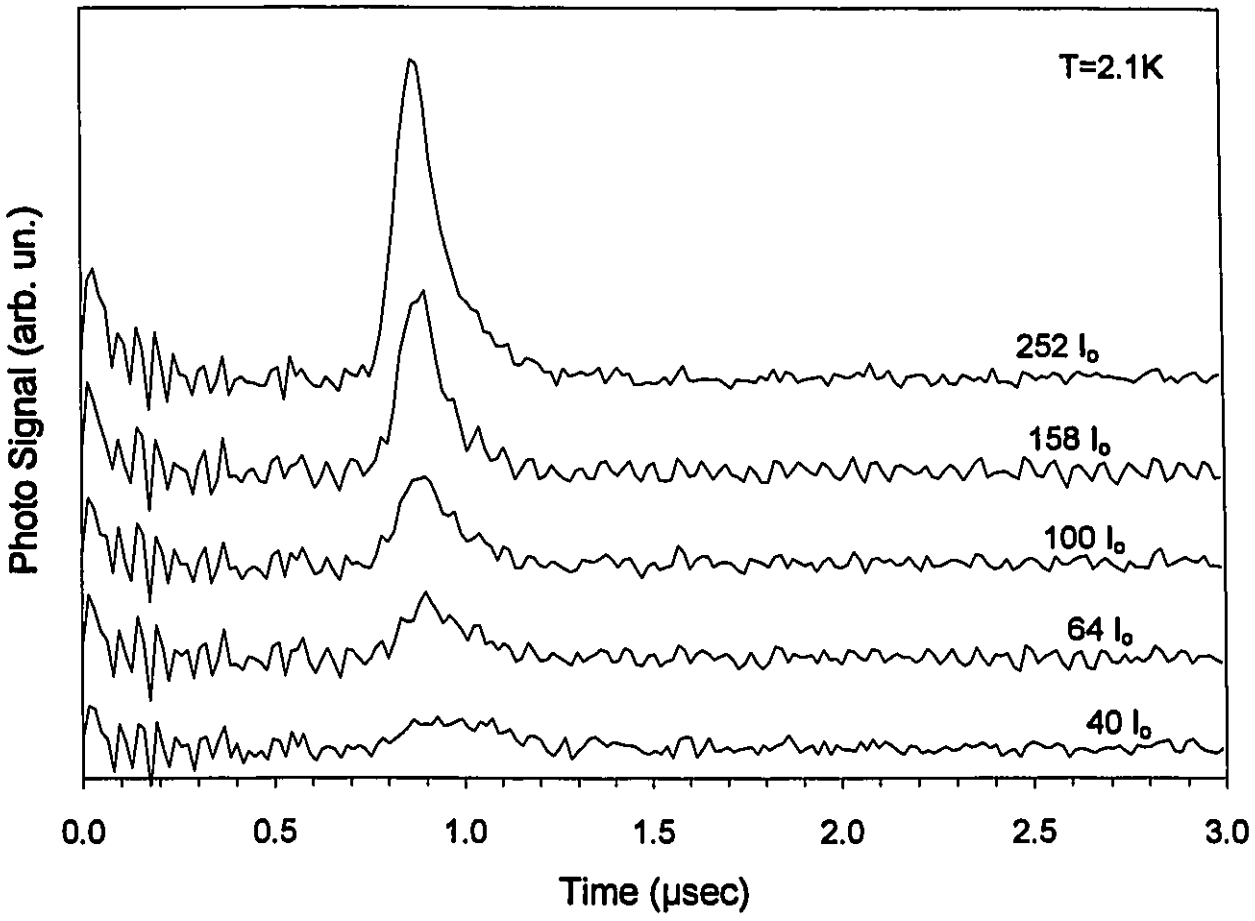

Fig. 26 Photo signal obtained with a sample of thickness d=3.7 mm for various laser intensities at a fixed temperature of T=2.1K.

Despite the weaker signal amplitudes due the H20E epoxy contacts, sample 1 was used in a new type of experiment where the incident intensity was held constant while the temperature was varied. The measurements were performed in superfluid He for T<2.17K, and in He gas for temperatures above 2.17K. The temperature in the gas was very difficult to control and the temperature attributed to a particular trace in Fig 26 is the average temperature over the acquisition time (~20 sec) of that trace. In previous measurements the temperature was measured before and after the waveforms were acquired and the temperature sensor would be disconnected during the acquisition. This would be impractical for the current experiment and so the background noise is thus increased by the constant use of the thermometer. Despite the experimental difficulties, a clear shift of the packet to later times and a widening of the exciton distribution is visible

as the temperature is raised only a few degrees. The behaviour is analogous to results obtained in the previous experiment, where the intensity is varied at fixed temperature, and again cannot be explained by classical diffusion theory. Such a small change in the temperature does not greatly affect the diffusion coefficient as seen in section 3.1.1, and the results in Fig. 27 clearly show a dramatic difference in the velocity and packet width in the traces at 2.1K and 4.1K.

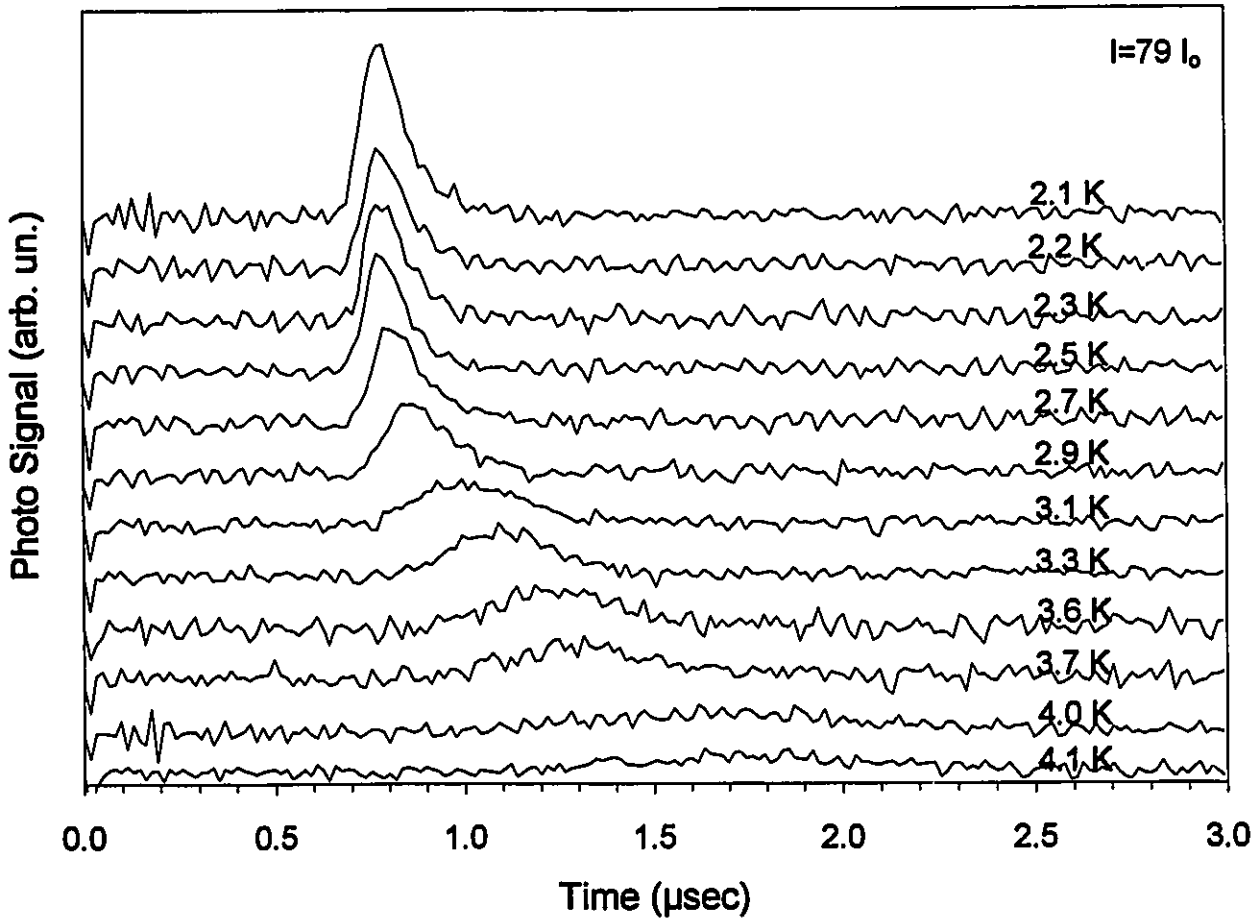

Fig. 27 Photo signal obtained with a sample of thickness d=3.28 mm for various temperatures at a fixed intensity 79 I_o.

The temperature sensor was left in place for all the following measurements to better correct for random temperature shifts which plagued earlier results. The increased noise was countered by better shielding in critical areas such as around the coaxial connectors on the cryostat and oscilloscope. Also more frequent background acquisitions

were made, and post acquisition processing techniques, such as smoothing, were improved.

Both samples were polished and etched to remove the CuO formed from the epoxy curing cycle and the "finger" type electrodes were replaced with the circular pattern as shown in Fig. 13b. The Silverprint compound which dried at room temperature was used as the wire bond. The signal amplitude was increased by nearly a factor of 2 over the initial results shown in Fig. 25. However a new problem was encountered that was avoided, unknowingly, in previous experiments. If laser light directly hit the electrodes, a front cell signal was recorded; however, there was a possibility that part of delayed exciton signal would be recorded with opposite polarity as is evident in Fig. 28, or, in some cases, no signal would be measured at all. The mechanism behind this effect is unclear but may be related to a transient photoelectric effect [30] caused by the creation of carriers by the scattered light near the Cu and Au layers. A second generation sample holder was thus constructed where the electrodes would be completely shielded from all stray light. The front cell photo signal was not necessary at this point since the time base was calibrated from previous measurements for the cryostat position.

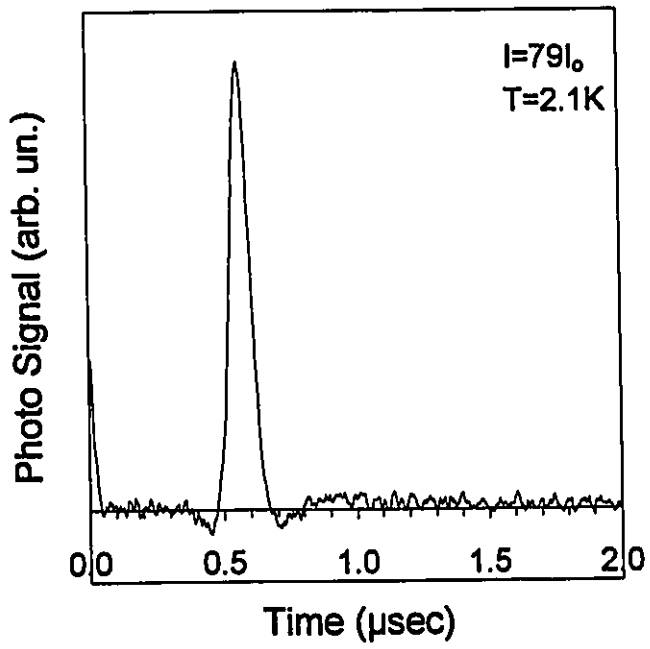

Fig. 28 Photo signal obtained with a sample of thickness d=2.2 mm.

Figure 29 displays a set of results obtained with sample 1 and the second generation sample holder as a function of incident intensity at a fixed temperature of T=2.1K. The behaviour is similar to that

observed under similar conditions in Fig. 25: the peak velocity increases and the packet size decreases as the intensity is raised, until a saturation point. The arrival time of the packet is smaller here due to a decrease in crystal thickness from the polishing, and the signal has gained a more symmetrical shape. The change in the shape of the signal may be due to the new type of electrodes, the circular pattern having a shorter fall time than the finger type electrodes. Or, more likely, the response time of the finger electrodes in the previous measurements was affected by scattered light as mentioned in section 3.1.2.

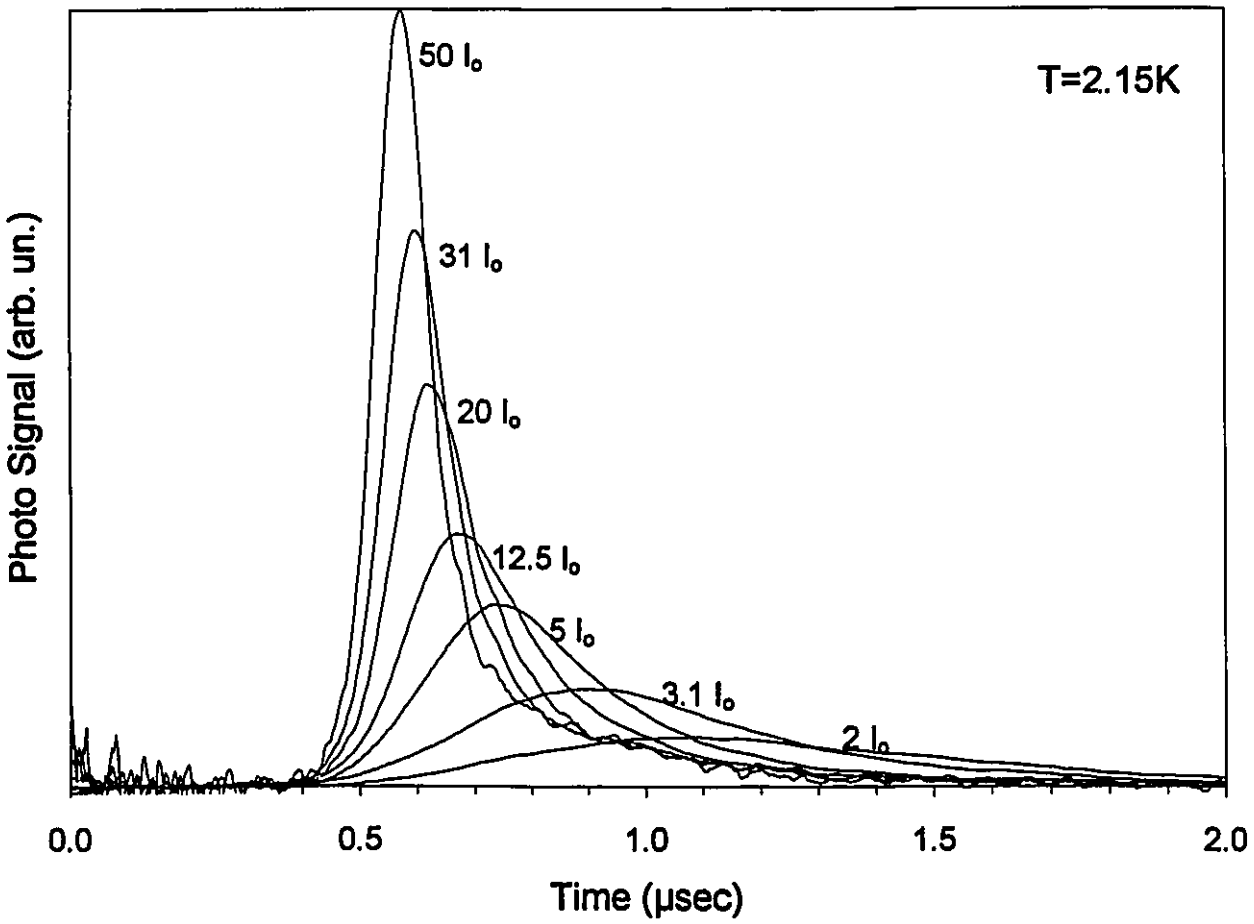

Fig. 29 Photo signal obtained with a sample of thickness d=2.2 mm for various intensities at a fixed temperature T=2.15K.

Again, using the second generation electrodes and sample holder, the signal was measured as a function of temperature at fixed intensity as in Fig. 27. The results in Fig.

30 were very impressive due to the larger signal amplitude and again a sharp temperature dependence of the packet velocity and size is obvious over the relatively small temperature range.

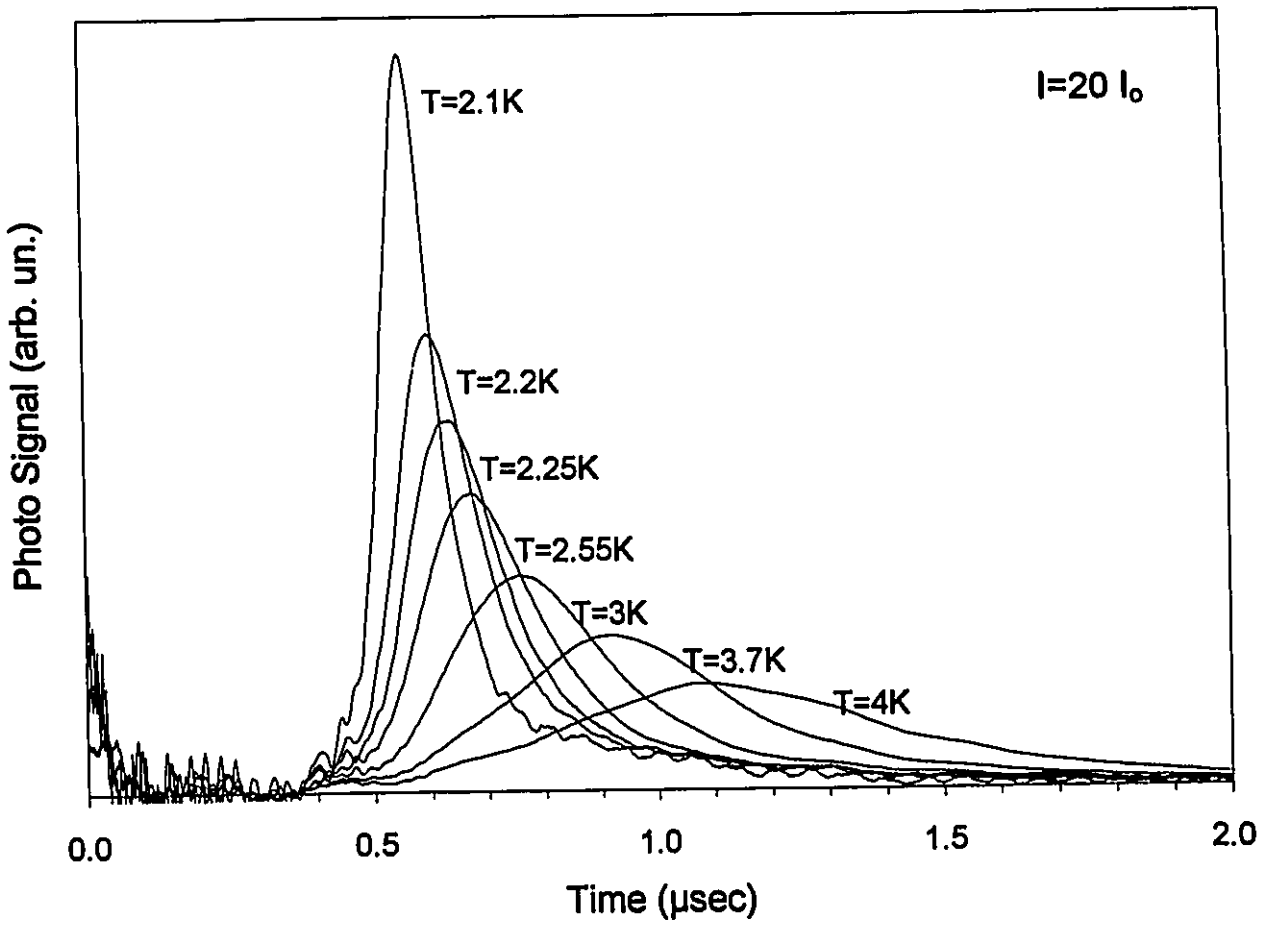

Fig. 30 Photo signal obtained with a sample of thickness d=2.2 mm for various temperatures at a fixed intensity 20 I_o.

To demonstrate the similar behaviour of the signal as a function of either temperature or density, Fig. 31 was constructed; it compares part of the results from Fig. 25 with some of the results shown in Fig. 30. The analogous evolution of the excitonic signal as a function of density and temperature in Fig. 30 is striking, and suggests that the changes seen in density and temperature are interrelated through a single physical process.

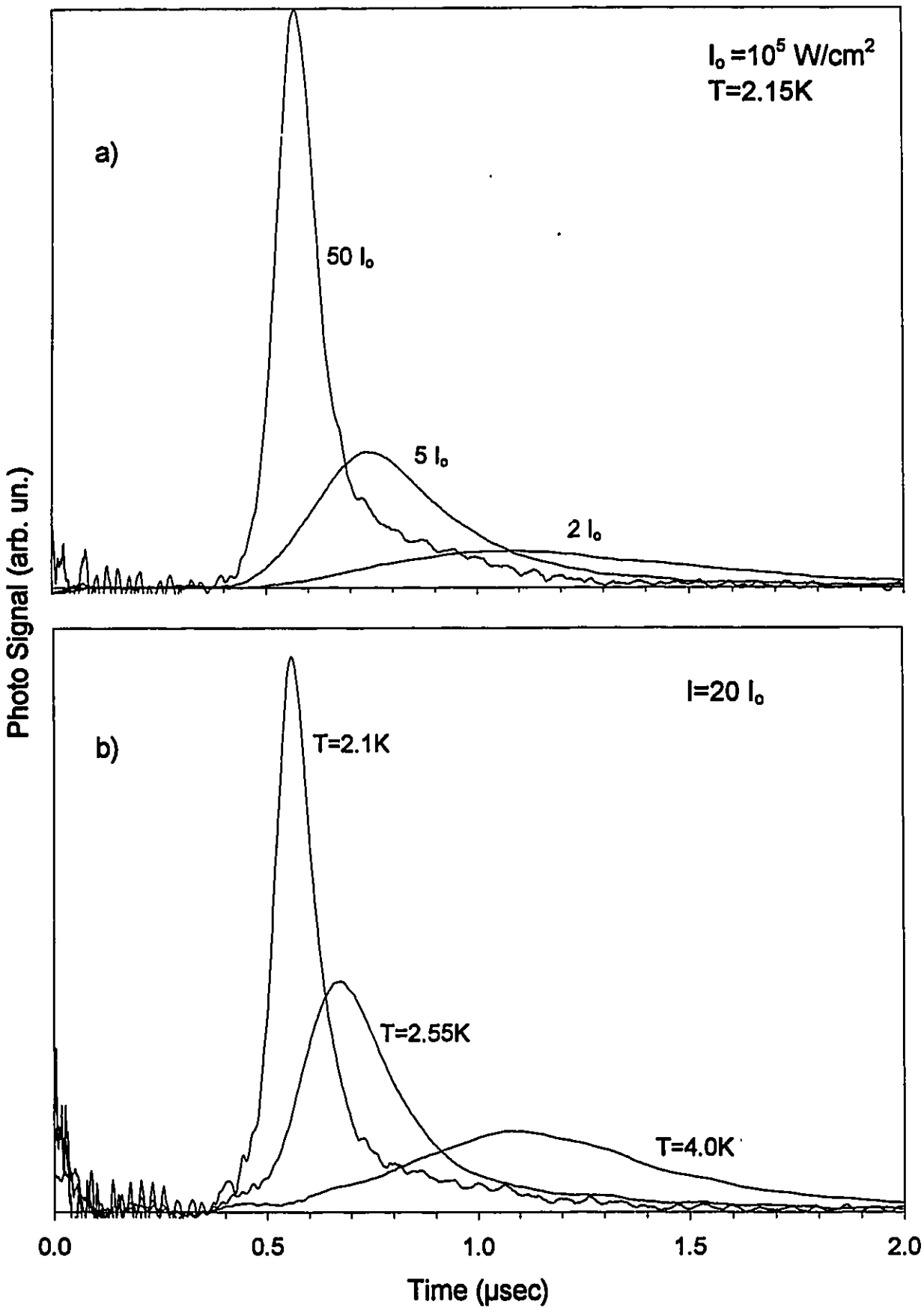

Fig. 31 Photo signal obtained with sample of thickness d=2.2 mm. a) at fixed temperature, b) at fixed intensity.

3.1.4 Phase Diagram

Following the success of the preceding experiments and the obvious sharp temperature dependence of the phenomena, the ensuing experiments aimed to map out the saturation point as a function of temperature and incident intensity and construct a phase diagram I_c vs T where I_c is the critical intensity at which there is a saturation point or break in the exciton transport.

After comparing the results from many different measurements at fixed intensity to many fixed temperature experiments, it was decided that future measurements used to map out the evolution of the break in the photo signal behaviour (i.e. saturation point) would be performed at fixed temperature. Experiments at constant temperature are more efficient with respect to Helium consumption since stabilizing the sample temperature can be a time and helium consuming process. Therefore once a particular temperature is achieved, it is more logical to make as many measurements as possible. Furthermore, complications could arise during the analysis of the fixed intensity measurements. The transition in the packet behaviour observed in Fig. 30 may become contaminated by an experimental artifact. The incident laser intensity is affected by bubbles in the liquid Helium near the λ-point, and therefore, an artificial break in the behaviour may be convoluted with the real physical changes in the signal behaviour.

Figure 32 is an example of one the many high temperature measurement sets obtained for the phase diagram to be shown in section 3.1.4 of the exciton gas transition. The same qualitative changes such as velocity shift and packet size reduction are observed at this temperature, although at a higher incident intensity.

To quantitatively evaluate the intensity at which a transition in the exciton gas behaviour occurs, the packet velocity (normalized to the speed of sound in Cu_2O) and the HWHMx2 were plotted as a function of intensity in Fig. 33. At low exciton density the cloud is rapidly expanding with a highly density dependent expansion coefficient as witnessed by the steep slope of the HWHMx2. However, at a critical intensity I_c (denoted

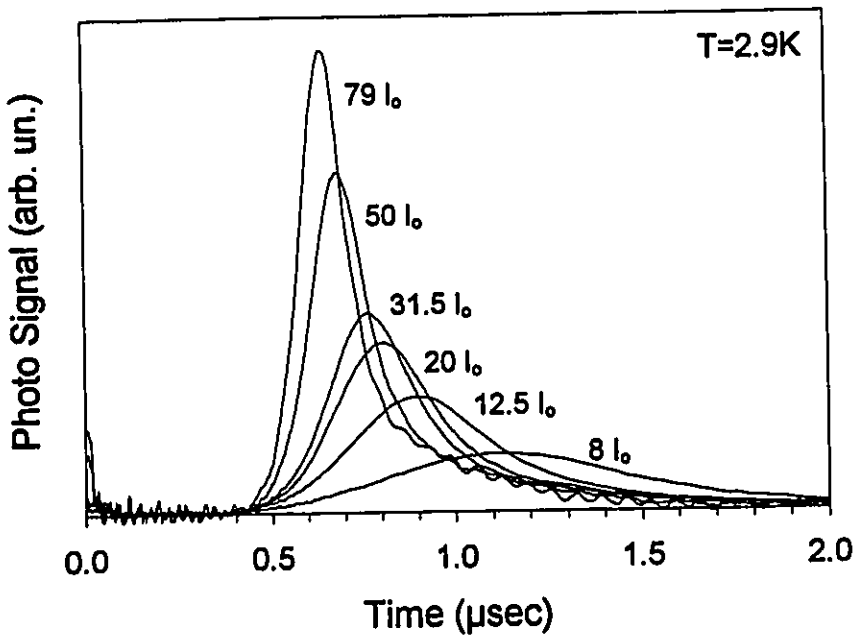

Fig. 32 Photo signal obtained with a sample of thickness d=2.2 mm for various intensities at a fixed temperature T=2.9K.

by the arrow), the behaviour changes and the slope of the HWHMx2 as a function of intensity suddenly decreases to nearly zero.

The same type of analysis was performed for all the other temperatures; several are shown for comparison in Fig. 34. As can be seen, as the temperature is increased, the critical intensity increases, and apparently so does the saturation point of the HWHMx2 (the smallest HWHMx2 that can be achieved for a particular temperature). There will be some error in the interpretation of I_c due to human judgement, especially when I_c falls between two steps in incident intensity, or if some of the data points are shifted due to noise

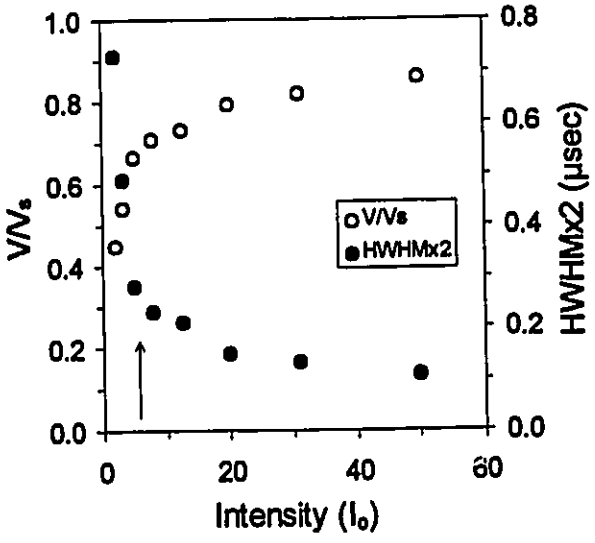

Fig. 33 HWHMx2 (filled circles) of the leading edge of the temporally resolved photo signal as a function of laser intensity at a fixed temperature T=2.1K. Velocity of the packet (open circles) normalized to the sound velocity in Cu_2O (v_s=4.5·10^5 cm/s).

in the original waveform, small changes in beam alignment or temperature fluctuations. At high intensities, the temperature shifts along the isotherms were kept to a minimum by reducing the repetition rate of the laser; in spite of this precaution some small steps may still be visible.

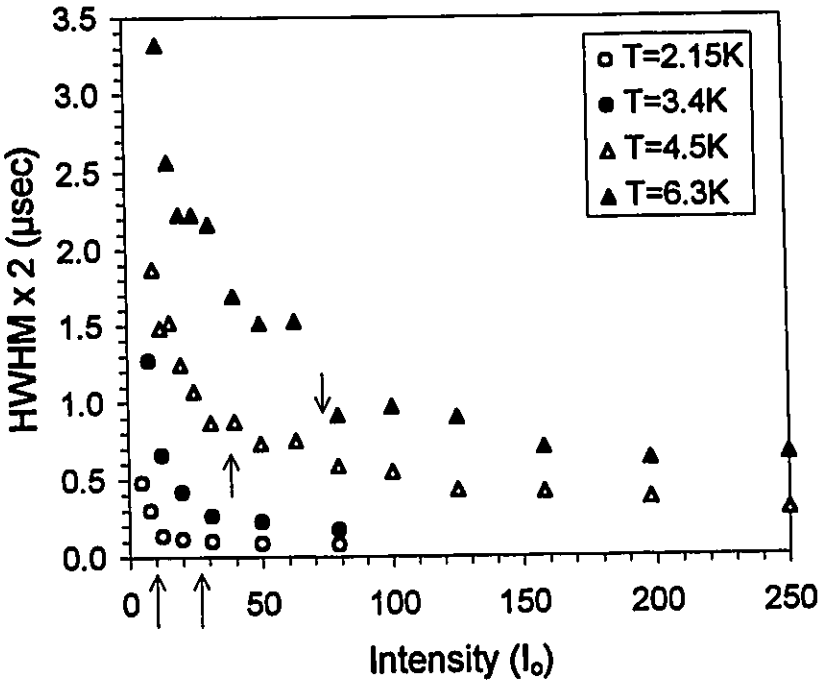

Fig. 34 HWHMx2 of the leading edge of a temporally resolved photo signal as a function of laser intensity at different sample temperatures.

The overall results of the above analysis are shown in Fig. 35, where the critical intensity is plotted as a function of temperature with error bars imposed by the uncertainties mentioned above. A line proportional to $T^{3/2}$ fitting the data points is also shown on the graph; the fitting coefficient a was 4.5. The $T^{3/2}$ dependence of the critical intensity suggests that the break or transition point is somehow related to the Bose-Einstein condensation of excitons. As well, the observed ballistic transport is consistent with superfluid behaviour associated with BEC. The narrowing of the packet at high intensities is again compatible with the Bose condensation model. Since BEC is in momentum space, all the particles in the condensate must have the same momentum and

the spreading of the cloud by classical particle diffusion is eliminated.

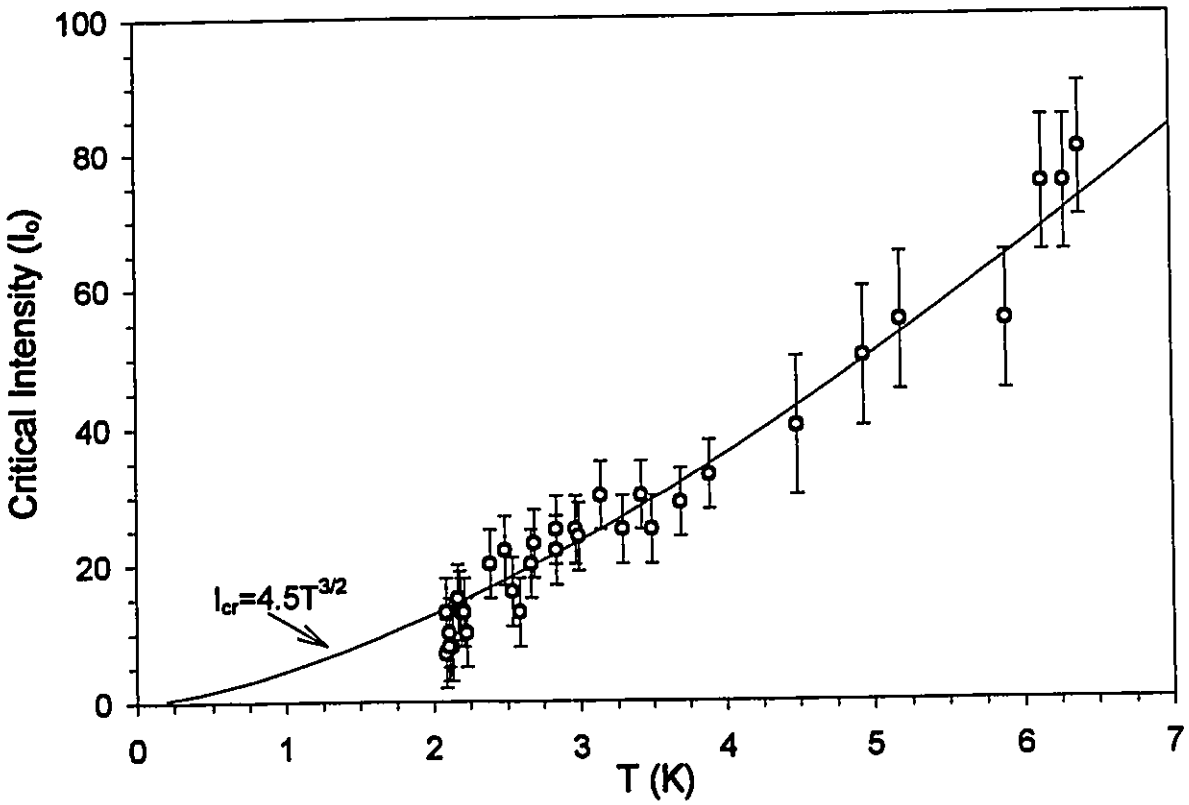

Fig. 35 Critical intensity as a function of sample temperature. The solid is a best fit of data (open circles) using a $T^{3/2}$ dependence and a fitting coefficient of 4.5.

We must now relate the intensity of the exciting laser light to the density in the exciton packet. At early times after the laser pulse the average density in the cloud is $\approx 0.44N_o\alpha/A$ as calculated in section 3.1.2. An intensity of $10I_o=10^6$ W/cm^2 corresponds to $N_o=6.5\cdot10^{14}$ photons at λ=532 nm; this leads to a density of excitons on the order of $3\cdot10^{19}$ cm^{-3}. Again it should be mentioned that the above density is quite similar to the value obtained at similar laser intensities in previous luminescence measurements where density values could be extracted from spectroscopic analysis [4]. Using this approximate method for the conversion of laser intensities to exciton densities we find a linear relationship between I and n and the critical temperature follows a $T^{3/2}$ dependence with the critical density. However the fitting coefficient a for the $T^{3/2}$ line in Fig. 35 is 500 times too large.

As an example, the critical intensity at 2K is about $10I_o$ as can be seen in Fig. 35. This intensity corresponds to a exciton density of $3 \cdot 10^{19}$ cm^{-3} while the predicted density for Bose condensation of the exciton gas at this temperature is $8 \cdot 10^{16}$ cm^{-3}.

A second method of estimating the density in the exciton cloud is to assume that almost all the excitons created in the crystal are in the packet arriving at the electrode face since the exciton lifetime is long compared to the transit time, and to divide the total number of excitons by the volume of the cloud. Using a cloud thickness of 700 μm (calculated at I_c from Fig. 33: thickness equals cloud velocity times HWHMx2) and a cloud area equal to the illuminated area A, the density in the packet at 2K is calculated to be $3 \cdot 10^{17}$ cm^{-3}, only four times larger than the predicted value $8 \cdot 10^{16}$ cm^{-3}. The relatively small discrepancy can be attributed to a combination of factors such as lateral expansion and surface recombination losses [31, 32, 33] neglected in the calculations.

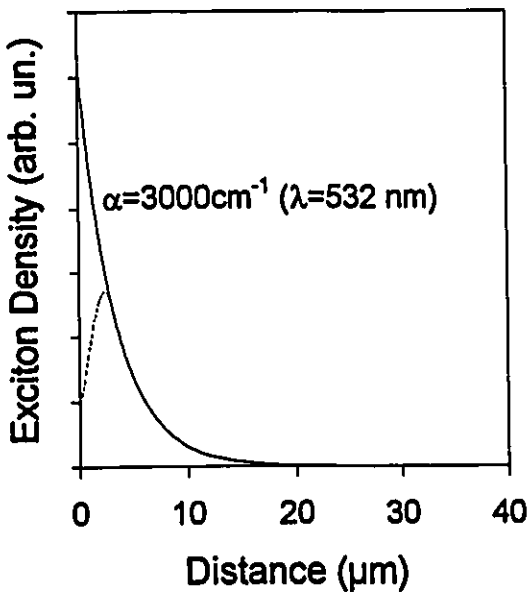

Fig. 36 Theoretical exciton density (solid line) as function distance from the sample surface for α=3000 cm^{-1}. Reduced exciton density (dotted line) from surface recombination.

Crystal defects which are more prevalent near the surface, provide recombination sites for the excitons. The high densities near the surface are attenuated by recombination and the total amount of excitons is reduced as shown qualitatively by the dotted line in Fig. 36. The expansion from the compact initial distribution of a few μm in thickness, to the large exciton cloud at later times can be explained by a substantial growth of the cloud during and soon after the laser pulse as mentioned in section 3.1.2. Therefore, including the effects mentioned above, the calculated density in the packet at low temperature agrees with the Bose model prediction. However the temperature

dependence of the cloud size at the critical intensity (see Fig. 34) makes for a non-linear relationship between I_c and n_c, and n_c will not follow the predicted $T^{3/2}$ dependence, but more a $T^{5/2}$ dependence in line with the critical pressure as function of temperature. The origin of the cloud expansion as a function of temperature is not clear and further experiments must be performed to adequately explain this behaviour.

To summarize, the excellent agreement of the experimental critical intensities with the $T^{3/2}$ fit and the initially linear relationship between intensity and density supports Bose-Einstein condensation of the excitons while the ballistic transport over macroscopic distances is an indication of their superfluid transport through the crystal. The initially over-estimated densities and the temperature dependence of the minimum packet width may be due to the ignorance of dynamical aspects of the evolution of the exciton cloud at early times. Many groups are currently working on models to overcome these problems [34].

3.2 Double Pulse Excitation

The double pulse or pump-probe experiments were devised to explore the interaction between two exciton clouds moving through the crystal and the effect of a condensate on non-condensed excitonic particles. All of the experiments were performed with sample 1 with finger type electrodes and the first generation sample holder, although the sample thickness did vary from one experiment to the next due to polishing.

3.2.1 Interaction between Packets

The following measurements explore the interaction between two packets of excitons separated by a small distance relative to their size. Figure 37 shows the photo signals observed in a sample of thickness d=2.65 mm held at 2.1K. Trace i) of Fig. 37 is obtained when the pump pulse alone irradiates the sample. The peak of the signal appears at a time delay $\Delta t \approx 0.6$ μsec yielding a packet velocity of $4.4 \cdot 10^5$ cm/s close to the speed of sound in the crystal and so this exciton packet can be considered to be in a condensed

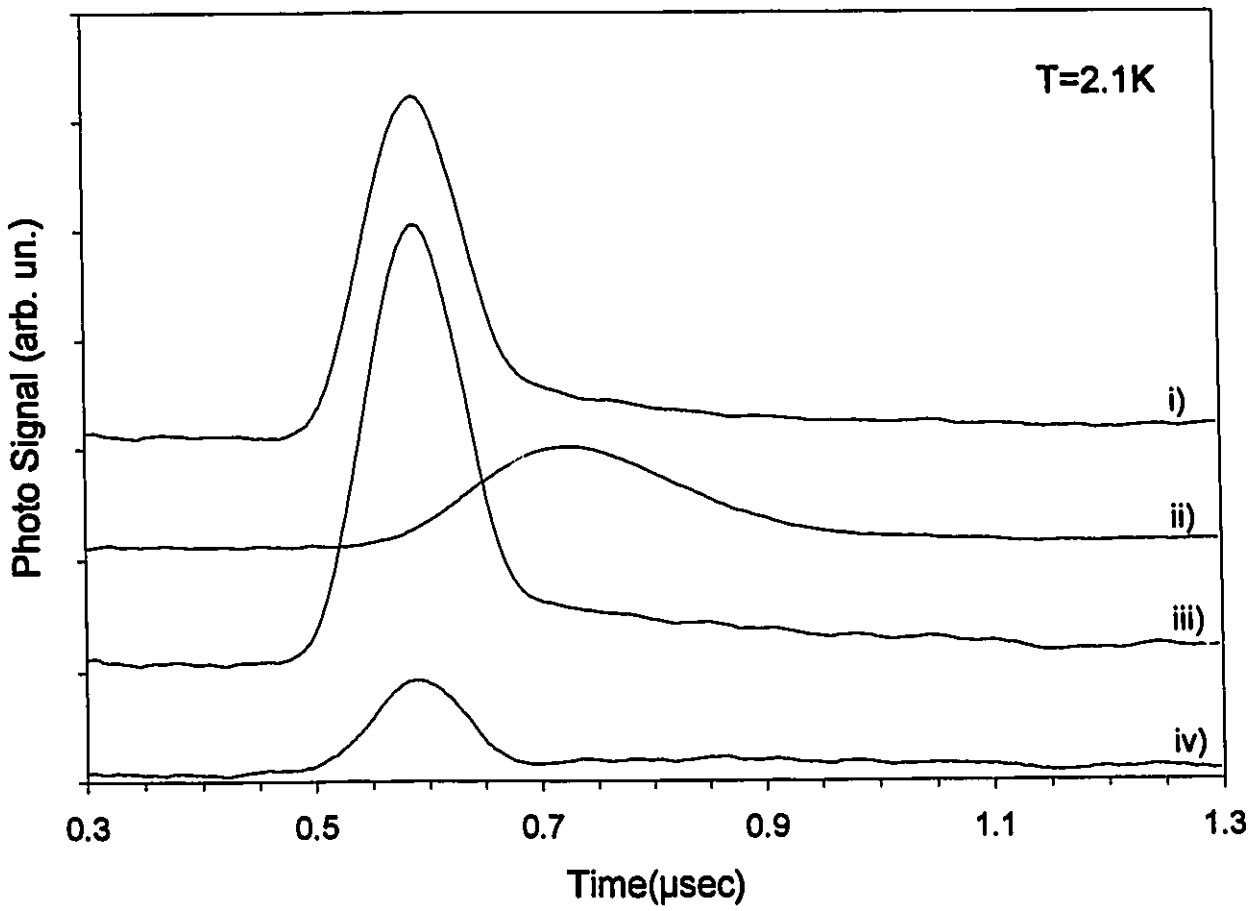

Fig. 37 Photo signal obtained with a sample of thickness d=2.65 mm at a fixed temperature T=2.1K.

state. Trace ii) corresponds to the signal from the weaker probe optical pulse alone. The photo signal has a larger time spread and the peak appears later, reflecting the diffusive motion of the particles. Trace iii) displays the signal measured when pump and probe pulses illuminate the sample sequentially with a time interval of δt=20 nsec between the two excitation pulses, slightly longer than the duration of each laser pulse. In trace iv) the signal obtained by subtraction of trace i) from trace iii) is plotted to better display the transport of the probe particles injected in the wake of the pump pulse. The differential signal is different from trace ii); instead of a diffusive motion, it displays the same ballistic transport as in trace i). The diffusive particles are being collected into the condensate as predicted by Bose theory since, once there is formation of a condensate, Bose particles are easily added to it.

A similar attractive effect is also seen in Fig. 38, which shows the photo signal obtained at a larger delay δt=125 nsec between the pump (i) and probe (ii) pulses of nearly equal intensity. The sequentially illuminated signal (iii) is larger than the algebraic sum of the signals from the individual packets (iv) reflecting the probe's ability to attract diffusive excitons left behind by the pump pulse. In this case the two condensates are close enough to merge together to from a single packet.

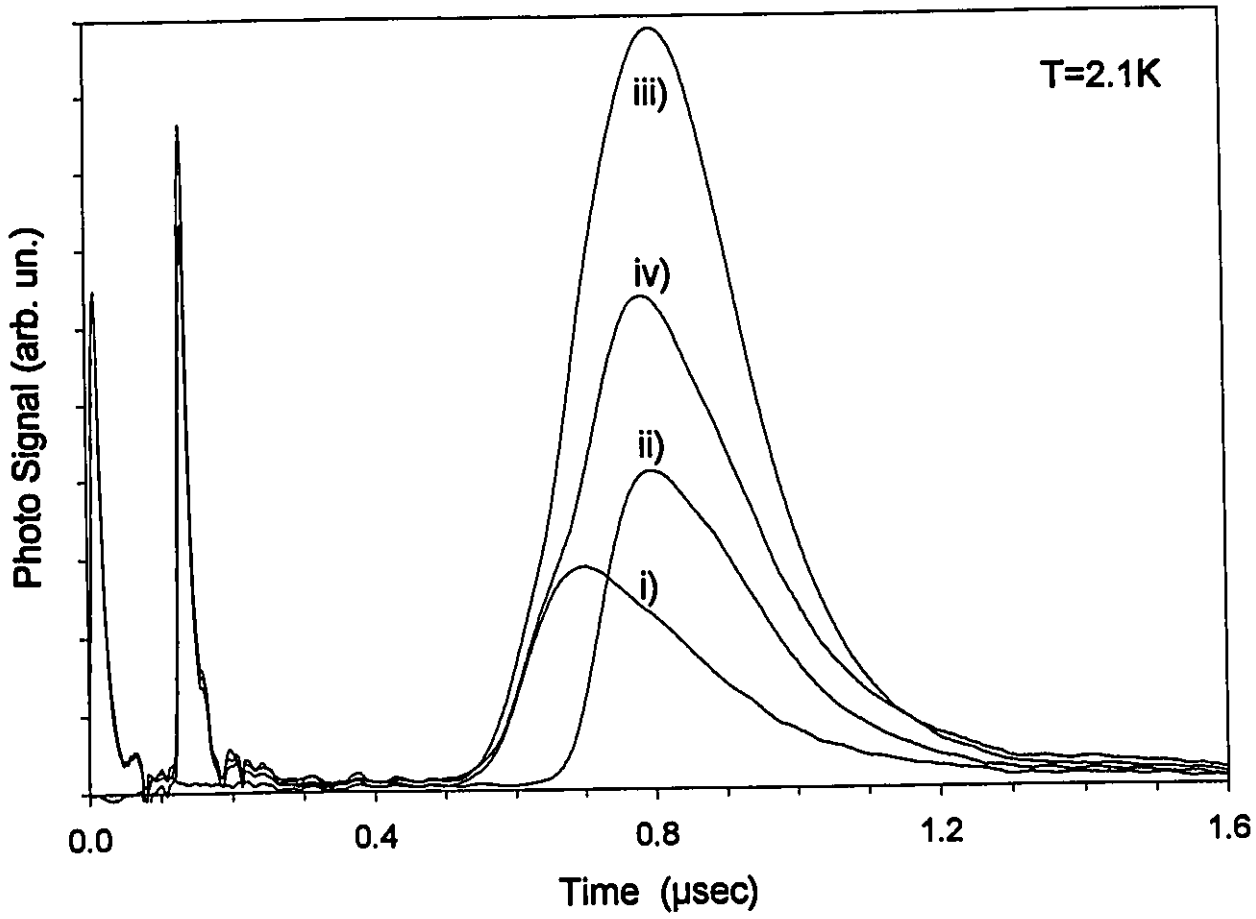

Fig. 38 Photo signal obtained with a sample of thickness d=2.5 mm at a fixed temperature T=2.1K.

3.2.2 Formation of a Condensed Soliton

We now study the propagation of a probe pulse population injected at still later times to investigate the interaction of two widely separated exciton packets. Results obtained in a crystal of thickness d=2.50 mm are shown in Fig. 39 for a delay of δt=278

nsec. Here the probe pulse is weaker than the pump pulse by a factor of 30; the corresponding diffusive signal is barely perceptible (trace ii). When the pump and probe pulses illuminate the sample sequentially, the probe-induced-signal is significantly modified (trace iii), collecting all the thermal excitons left behind by the pump. It takes the form of a packet (trace iv = trace iii - trace i) moving at $v=d/\Delta t'=3\cdot10^5$ cm/s where $\Delta t'=0.84$ μsec is the time delay between the probe pulse and the peak of the secondary packet. This velocity is smaller than the speed of sound and therefore excludes a mechanism for exciton ballistic transport somehow associated with the presence of a phonon shock wave generated by the thermalization of the excitons from their initial energy to the n=1 paraexciton state.

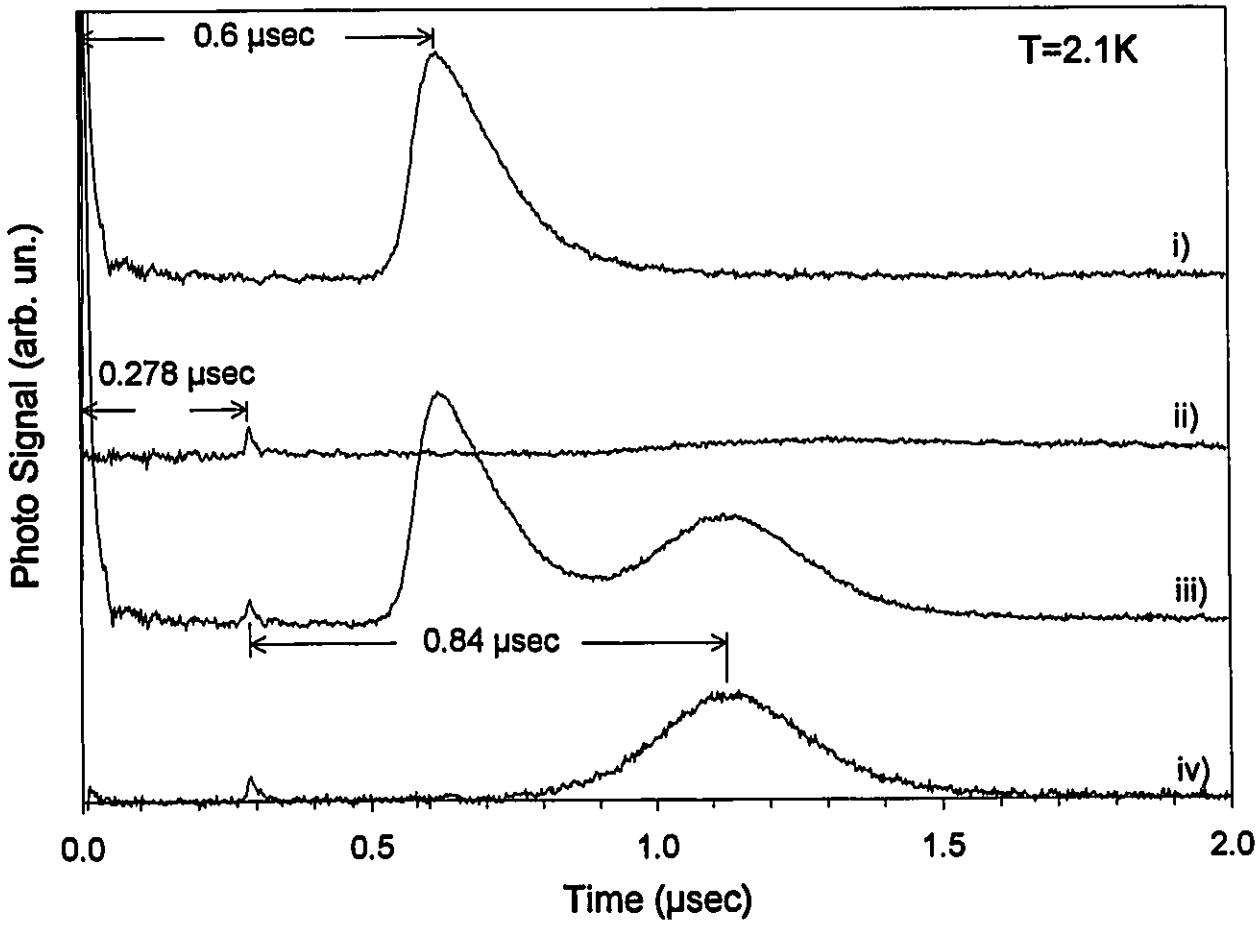

Fig. 39 Photo signal obtained with a sample of thickness d=2.5 mm at a fixed temperature T=2.1K.

When the probe pulse intensity is increased by a factor of 30 the number of particles in the secondary packet remains nearly constant, as shown in Fig. 40. This behaviour is typical of pulse amplification in a saturated gain regime [35]. In the present case, amplification of the photo signal is due to a transfer of particles created by the pump pulse towards the probe-induced packet. Thermal excitons left behind in the trail of the pump-induced packet are collected by the probe packet as it progresses through the sample.

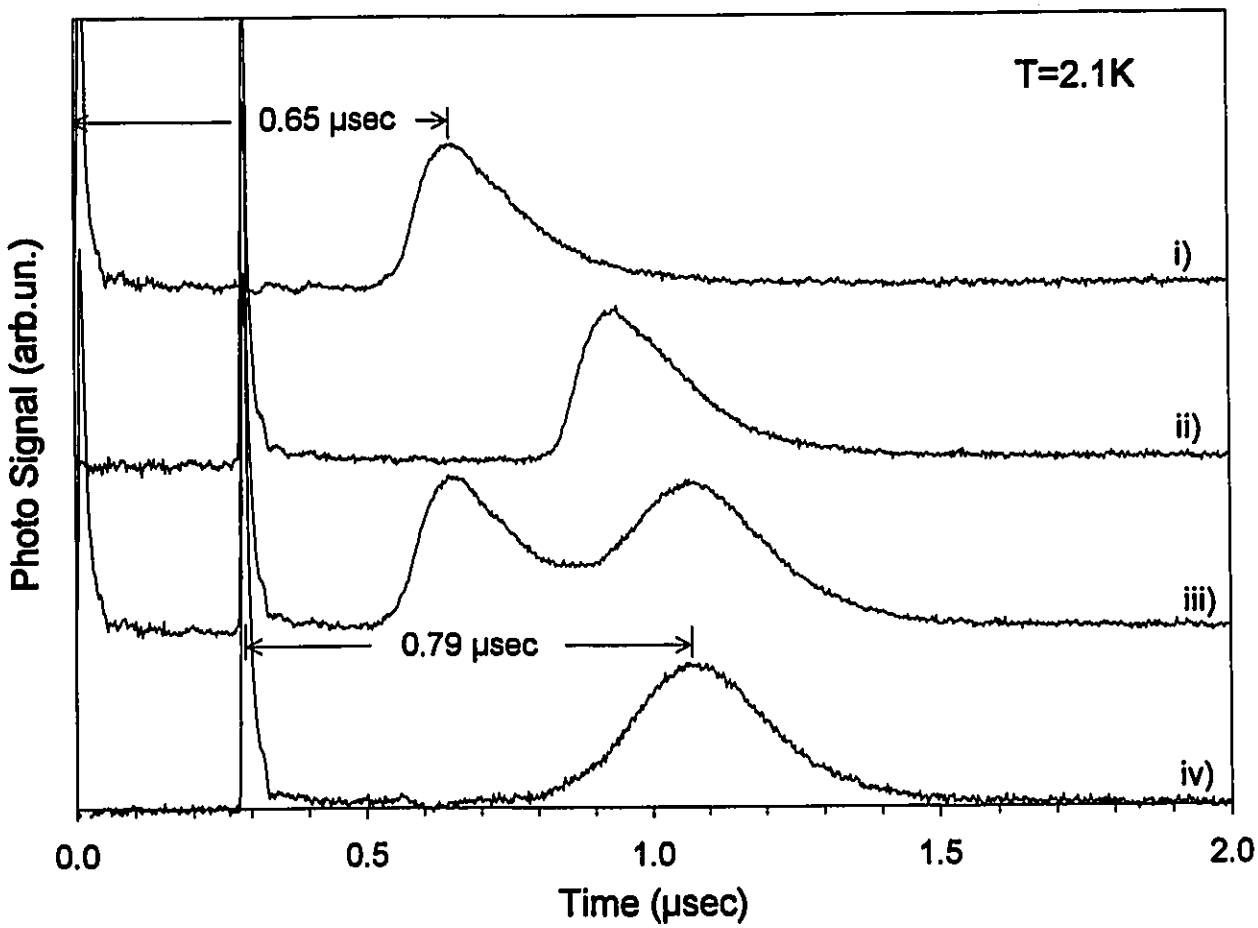

Fig. 40 Photo signal obtained with a sample of thickness d=2.5 mm at a fixed temperature T=2.1K.

The secondary packet was fitted with the following expression

$$\phi^2 = |\phi_o|^2 \operatorname{sech}^2\left(\frac{|R - vt|}{R_o}\right) \qquad (1)$$

which describes the time profile of an envelope soliton of lowest order. As can be seen in Fig. 41, Eq.(33) (open circles) fits the experimental data (solid line) exceptionally well with the parameters $v=2.98\cdot10^5$ cm/s: the speed of the packet, and $R_o=0.8$mm: the width of the packet. The dotted line in Fig. 41 is a best fit gaussian profile which does not model the data as well as Eq. (33). The value obtained for the width of the soliton and the magnitude of the signal are comparable to the values obtained with single pulse excitation at the critical intensity and at the same temperature; this suggests the soliton is Bose condensed.

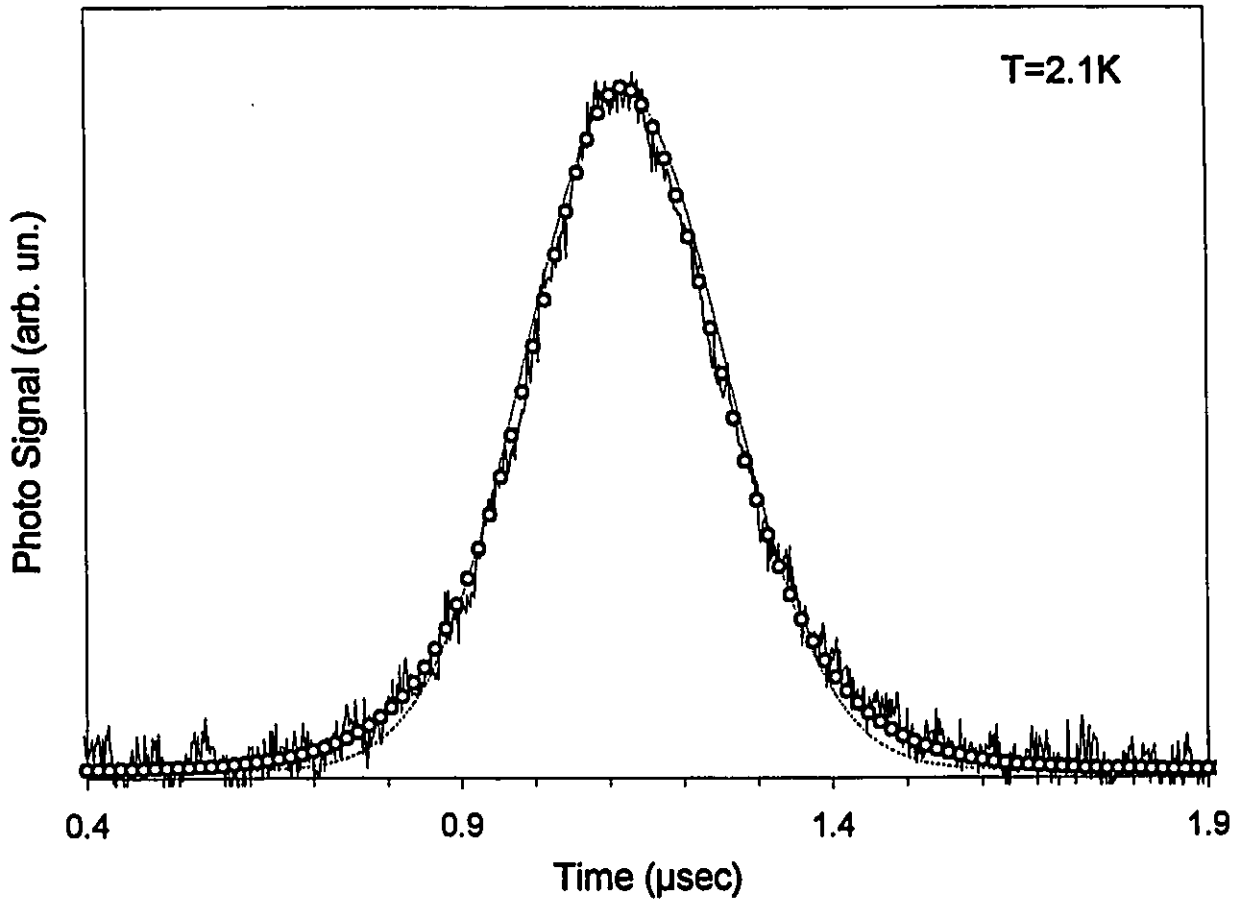

Fig. 41 Secondary packet (trace iv of Fig. 40) shown on expanded scale with a best fit to a $sech^2$ function (open circles). For comparison a best fit Gaussian profile (dotted line) is also shown.

From many other best fits obtained with different probe pulse intensities, the product of the peak height ($|\phi_o|^2$) times the square root of the width (R_o - FWHM) of the

secondary signal was found to be constant within 4% for a range of peak height of 1.4. The relation $(\phi_o R_o)^{1/2}$=constant constitutes another well known characteristics of solitary waves [36]. The perfectly time-symmetric packet is therefore interpreted as a solitary wave resulting from the attraction of thermal excitons into a Bose condensate, as well as the attraction between condensed excitons. The microscopic origin of the attractive force between condensed excitons at high densities and low temperature is discussed in [36]. The model proposed in [36] assumes the presence of a condensate propagating through a gas of thermal particles and predicts the formation of soliton-like exciton pulses.

Conclusions

The time resolved photo signal produced by the dissociation of excitonic particles at a Cu/Cu_2O interface on a natural growth high purity Cu_2O semiconducting crystal was used to monitor the transit through the crystal of long lived paraexcitons. The paraexcitons were created at the opposite face from the Cu/Cu_2O interface, several millimeters away, by a high intensity pulsed Nd:YAG laser. The time resolved results obtained at liquid helium temperatures show classical diffusion of excitons across the crystal at low excitation intensity hence low particle density. However above a critical exciton density for a fixed temperature, or below a critical temperature for a fixed density, the transport of the particles is not consistent with classical diffusion.

Above the critical density the particle transit velocity approaches the speed of sound $v_s=4.5\cdot10^5$ cm/s in the Cu_2O, and the concomitant of particle transit times measured at low exciton density is replaced by a compact cloud. The exciton cloud was measured traveling up to 8.3 mm with little or no dispersion of the particles. The apparent critical density (or temperature) mentioned above is attributed to a Bose-Einstein condensation of excitons. Condensed excitons are predicted to migrate unimpeded near the speed of sound through the crystal. The experimentally observed behaviour of the exciton cloud is consistent with the predictions of Bose statistics, and the temperature dependence of the critical intensity was verified to follow the predicted $T^{3/2}$ critical density dependence. The magnitude of the critical density in the exciton packet at the Cu/Cu_2O interface at low temperatures was also verified to match the predicted value for Bose condensation of paraexcitons in Cu_2O.

More measurements using two sequential pulses to illuminate the sample were performed to further investigate the behaviour of the condensate. For short pulse intervals an exciton condensate proved to be attractive for other non-condensed excitons as predicted in reference 36. For longer pulse delays, measurements revealed the formation

of a time-symmetric pulse as a condensate passed through a field of thermalized excitons. The time-symmetric pulse was well fitted with a soliton equation and its width and amplitude conformed to the predicted behaviour for a soliton.

Future efforts should include trying to get a better understanding of the exciton dynamics during and soon after the laser pulse. This might be done by computer modeling of the exciton population. The effects of changing the initial exciton distribution by varying the incident laser wavelength and hence changing the absorption coefficient in future experiments might also help explain the evolution of the exciton cloud. And finally the effect of a constant background field of excitons on the condensate could be further studied by illuminating the crystal with a cw laser which has a wavelength corresponding to a small absorption coefficient.

References

1. D. W. Snoke, J. P. Wolfe and A. Mysyrowicz, Phys. Rev. Lett. 64, 2543 (1990).
2. D. Hulin, A. Mysyrowicz and C. Benoît à la Guillaume, Phys. Rev. Lett. 45, 1970 (1980).
3. D. Snoke, J. P. Wolfe and A. Mysyrowicz, Phys. Rev. Lett. 59, 827 (1987).
4. D. Snoke, J. P. Wolfe and A. Mysyrowicz, Phys. Rev. B 41, 11171 (1990)
5. A. Mysyrowicz, D. Snoke and J. P. Wolfe, Phys. Stat. Sol. B 159, 387 (1990).
6. I. Pasternyak, Soviet Phys. Solid State 1,888 (1959).
7. A. Mysyrowicz, D. Hulin and A. Antonetti, Phys. Rev. Lett. 43, 1123 (1979).
8. N. Caswell, J. S. Weiner and P. Y. Yu, Solid State Commun. 40, 843 (1981).
9. D. W. Snoke, A. J. Shiels and M. Cardona, Phys. Rev. B. 45, 11693 (1992).
10. A. I. Bobrysheva and S. A. Moskalenko, Phys. Status Solidi B 119, 141 (1983). A. I. Bobrysheva, M. F. Miglei and M. I. Shmiglyuk, Phys. Status Solidi B 53, 71 (1972).
11. F.Bassani and M. Rovere, Solid State Commun. 19, 887 (1976).
12. N, Peyghambarian, L. L. Chase and A. Mysyrowicz, Phys. Rev. B 27, 2325 (1983).
13. A. Mysyrowicz, private communication.
14. Jia Ling Lin and J. P. Wolfe, Phys. Rev. Lett. 71, 1222 (1993).
15. L. V. Gregor, J. Chem. 66, 1645 (1962).
16. Ye Wang, MSc. Thesis, University of Ottawa (1991).
17. A. I. Bobrysheva, S. A. Moskalenko, S. S. Russu and M. I. Shmiglyuk, Phys. Solid State 36, 1098 (1994).
18. E. Tselepis, E. Fortin and A. Mysyrowicz, Phys. Rev. Lett. 59, 2107 (1987).
19. L.C. Olsen and R.C. Bohara, Appl. Phys. Lett. 34, 47 (1979).
20. E. Fortin and W.M. Sears, Can. J. Phys. 60, 901 (1982).
21. J. Bardeen, Phys. Rev. 71, 717 (1947).

22. A. Mysyrowicz, D. Hulin and E. Hanamura, in *UltraFast Phenomena VII*, (Springer, Berlin, 1990).

23 A. A. Berezin and F. L. Weichman, Phys. Stat. Sol. A 71, 265 (1992).

24 L. C. Olsen, F. W. Addis, and W. Miller, Solar Cells, 7. 247, (1982-1983).

25. D. P. Trauernicht, J. P. Wolfe and A. Mysyrowicz, Phys. Rev. Lett. 52, 855 (1984).

26. D. P. Trauernicht and J. P. Wolfe, Phys. Rev. B 33, 8506 (1986).

27. J. Bardeen and W. Shockley, Phys. Rev. 80, 72 (1950).

28. M. A. Tamor and J. P. Wolfe, Phys. Rev. Lett. 44, 1703 (1980), and Phys. Rev. B 26, 5743 (1992).

29. B. Link and G. Baym, Phys. Rev. Lett. 69, 2959 (1992).

30. Solomon Meerovich Ryvkin, *Photoelectric Effects in Semiconductors*, Consultants Bureau, New York, (1964)

31. Alain Barbarie, Ph.D. Thesis University of Ottawa, p68-69 (1974).

32. D. L. Lile, Phys. Rev. B 8, 4705 (1973).

33. B. Karlsson, C. G. Ribbing, A. Roos, E. Valkonen and T. Karlsson, Physica Scripta 25, 826 (1982).

34. *Bose-Einstein Condensation*, Cambridge University Press, edited by A. Griffin D. W. Snoke and S. Stringari, 1995.

35. A. Hasegawa, *Optical Solitons in Fibers*, Springer Tracts in Modern Physics 116 (Springer-Verlag, Berlin, 1989).

36. E. Hanamura, Solid State Comm., 91, 889 (1994).